JOHANNES KEPLER
UNIVERSITY LINZ

Author
Stefan Pöllner BSc

Submission
Institute of Physical Chemistry and Linz Institute of Organic Solar Cells

Thesis Supervisor
a. Univ. Prof. Dr. Markus Scharber

Co-Supervisor
DI[in] Katarina Gugujonović

March 2022

A processable and efficient perovskite solar cell with a large band gap

Master Thesis

to obtain the academic degree of

Diplom-Ingenieur

in the Master's Program

Chemistry and Chemical Technology

JOHANNES KEPLER UNIVERSITY LINZ
Altenbergerstraße 69
4040 Linz, Austria
www.jku.at
DVR 0093696

Acknowledgement

I would like to thank my supervisor a. Univ. Prof. Dr. Markus Scharber for the numerous feedback and for the constructive advices how to layout graphs and to structure my written master thesis. I want to thank my co-supervisor DI^{in} Katarina Gugujonović for introducing me into the craft of making perovskite solar cells and providing me very helpful and practice related tips for moving forward and improving my master thesis. My special thanks goes to o. Univ. Prof. Mag. Dr.DDr. h.c. Niyazi Serdar Sariciftci for his inspiring lectures and for giving me the opportunity to do my master thesis in his institute and with his great team.

It is an important concern for me to thank my colleagues Dr. Bekele Teklemariam for his various helpful ideas, how I can improve my perovskite solar cell production process, Dr. Cigdem Yumusak for introducing me into the technique of thermal fullerene-C_{60} evaporation, DI Jakob Hofinger for thoughtful discussion on the charge carrier transport model and the function of buffer layers, MSc Christoph Putz for introducing me how to use a antisolvent pump and MSc Lukas Lehner for his advices on the deposition of hole transport layers. I also want to thank Dr. Munise Cobet, Gabriele Hinterberger and Gerda Kalab for their unlimited support and for keeping the laboratory running. My very special gratitude belongs to DI Felix Mayr and Konstantin Siegel for the introduction in the very elegant technique of photo-thermal deflection spectroscopy, for all the inspiring discussions and for analysing my samples with this method. Finally, I want to thank the members of the LIOS team, for their aid in developing this thesis and for providing a nice atmosphere in the institute.

Last but not least, I want to express my deeply gratitude to my parents, my brothers, my girlfriend and my friends for their unconditional support in good and in bad times, for boosting my resilience and accepting and appreciating me as I am.

Abstract

Solar cells are a promising renewable energy source, due to the easy, global expandability and due to the expected dramatic increase in energy demand in the future. Perovskite solar cells have shown an impressive development towards a record power conversion efficiency of 25.6 % in 2021. Recently, perovskite solar cells with a large bandgap are gaining focus in research, as they can be used in light-emitting diodes and in tandem solar cells. They are utilized as absorber for high-energy photons, allowing the power conversion efficiency to overcome the theoretical Shockley-Queisser limit in tandem solar cells. Furthermore, perovskite solar cells show a bandgap tunability, which makes them optimal candidates for current matching in tandem solar cells. In this work, a recipe and processing procedure for a processable and efficient perovskite solar cell with a large band gap was implemented and progress was recorded with current-voltage measurements. Furthermore, the influence of the bromide proportion in the halide fraction of the perovskite onto the band gap was revealed and the photostability and phase segregation of perovskites was investigated. A champion-perovskite solar cell with an band gap of 1.73 eV, a power conversion efficiency of 10.5 %, a fill factor of 61 %, an open-circuit voltage of 1.10 V and a short-circuit current density of 14.6 mA cm^{-2} was constructed. The photoluminescence and electroluminescence, the external quantum efficiency and surface morphology of the best perovskite solar cells was investigated.

Kurzfassung

Solarzellen sind aufgrund der leichten globalen Ausbaufähigkeit und des voraussichtlich drastisch steigenden Energiebedarf in der Zukunft eine vielversprechende, erneuerbare Energiequelle. Perowskit-Solarzellen zeigten in der Vergangenheit eine beeindruckende Entwicklung und erreichten im Jahr 2021 einen Wirkungsgrad von 25,6 %. In jüngster Zeit rückten Perowskit-Solarzellen mit einer großen Bandlücke in den Fokus der Forschung, da sie in Leuchtdioden und in Tandemsolarzellen als Absorber für hochenergetische Photonen eingesetzt werden können. In Tandemsolarzellen kann der Wirkungsgrad die theoretische Shockley-Queisser-Grenze überwinden. Darüber hinaus weisen Perowskit-Solarzellen eine Möglichkeit zur Adjustierung der Bandlücke auf, was sie zu optimalen Kandidaten für die Stromanpassung in Tandemsolarzellen macht. In dieser Arbeit wurde eine Rezeptur und ein Herstellungsverfahren für eine verarbeitbare und effiziente Perowskit-Solarzelle mit einer großen Bandlücke implementiert und der Fortschritt durch Strom-Spannung-Messungen aufgezeichnet. Darüber hinaus wurde der Einfluss des Bromidanteils in der Halogenidfraktion des Perowskits auf die Band-lücke aufgezeigt und die Photostabilität und Phasensegregation von Perowskiten untersucht. Die beste hergestellte Perowskit-Solarzelle erreichte eine Bandlücke von 1.73 eV, einen Wirkungsgrad von 10,5 %, einen Füllfaktor von 61 %, eine Leerlaufspannung von 1,10 V und eine Kurzschluss-Stromdichte von 14.6 $mA\,cm^{-2}$. Bei dieser Champion-Perowskit-Solarzelle wurde die Photolumineszenz, die Elektrolumineszenz, die Quantenausbeute und die Oberflächenmorphologie untersucht.

Contents

"*Following the light of the sun, we left the old world.*"

- Christopher Columbus

1 Introduction

A rapid growing world population and an increasing prosperity led to an enormous rise of word energy demand to 418 EJ in 2019 [1]. In order to achieve the goal of the Paris agreement 2015, to limit the mean global temperature to a maximum of 1.5 °C or at least 2.0 °C above pre-industrial levels, a dramatic increase of environmentally friendly renewable energy sources is required. Solar cells are a promising technology as there is more than enough sunlight to satisfy global energy demand and as photovoltaic modul costs decayed vigorously in the last decades [2]. In the year 2020, 821 TWh (≙ 2.96 EJ) energy was produced by PV modules [1]. Currently silicon based photovoltaic (PV) modules dominate the global market as they achieve high power conversion efficiencies (mono-crystalline Si 26.7 % in lab scale [3]) and have low prices ($0.30 W^{-1} photovoltaic capacity cost [2] and €0.055 kWh^{-1} - €0.07 kWh^{-1} cost of PV-energy in Germany in 2019 [2]).
Perovskite solar cells (PSC) are a promising emerging technology as they offer high power conversion efficiencies (*PCE*s), a low-temperature solution-processing method and an adjustable band gap (E_g) [4–7]. The heart of a PSC is a perovskite layer, which is a material class with a cubic-octahedral ABX_3 crystal structure, where A and B represent cations and X is an anion (see section 1.1.1) [8]. In 2009 the first PSC was reported with a *PCE* of 3.8 % [9]. In 2021 a PSC was reported with a record *PCE* of 25.6 %, which highlights the enormous progress in the development of PSCs in the last decade [10]. Additionally, perovskite solar cells with a large band gap ($E_g \geq 1.65$ eV) are under research. These can absorb high-energy photons and can be utilized in tandem solar cells (TSC) with multiple junctions to push *PCE* above the theoretical Shockley-Queisser limit of slightly above 30 % for single junction solar cells [11, 12]. Perovskites allow a simple band gap increase by cation- and halide(anion)-adjustment, which will be discussed in the following sections.

The aim of this thesis was to develop and produce a perovskite solar cell with a large band gap, to optimize the cell containing a multiple-cation, mixed-halide perovskite and to analyse the solar cell and the used materials with UV-VIS, photoluminescence (*PL*), current-voltage (*IV*) and external quantum efficiency (*EQE*) measurements. The mixed-halide PSC was designed for a band gap of 1.73 eV for following reasons: First, for band gaps that high photostability in PSCs can be achieved. Second, for this band gap a current match can be achieved with a 1.13 eV sub cell in tandem solar cells and third, the band gap can be tuned by adjusting the the bromide content of the perovskite. The core of this work was to investigate the effect of the bromide content in perovskites onto the band gap and photostability and moreover the implementation

and development of a recipe and processing procedure for a PSC with a large band gap. An analysis of perovskites and solar cells by photothermal deflection spectroscopy (PDS), *PL* and electroluminescence (*EL*) spectroscopy, scanning electron microscopy (SEM), *IV* and *EQE* measurements was performed.

1.1 Perovskite solar cell

1.1.1 Structure of a perovskite solar cell

The main component of a perovskite solar cell is a photoactive perovskite layer. The perovskite layer typically displays a thickness from 300 nm to 600 nm [13, 14], whereas commercial crystalline silicon layers in solar cells typically have a thickness around hundred micrometers [15]. Perovskites show a cubic-octahedral ABX_3 structure, which is illustrated in figure 1 (a). In hybrid organic-inorganic halide perovskites (OIHP), A represents an organic cation such as methylammonium (MA), formamidinium (FA) or a monovalent metal cation (as fraction) such as Cs^+. The B site typically consists of divalent metals like Pb^{2+} or Sn^{2+} and X symbolizes the halides I^-, Br^- or Cl^- [8, 16].

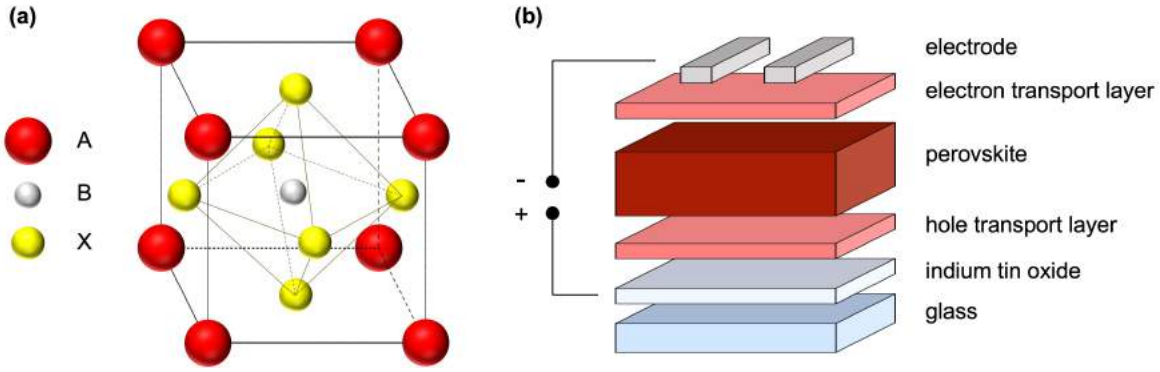

Figure 1: (a) Crystal structure of a organic-inorganic halide perovskite, where A is a large organic cation, B is a small divalent metallic cation and X is a halide. (b) Schematic structure of an inverted perovskite solar cell. From bottom to top: Glass, indium tin oxide as front electrode, HTL (PTAA), perovskite, electron transport layer (C_{60}:BCP or $PC_{60}BM$:BCP) and back electrode (Ag).

Depending on where the light enters a PSC, it is defined as a normal (negative-intrinsic-positive, n-i-p) or an inverted (p-i-n) structure. In a normal configuration the light travels trough the cathode/electron transport layer (ETL) to reach the photo-absorbing layer. In the inverted setup, it first hits the anode/hole transport layer (HTL). In both cases a transparent conductive oxide functioning as an electrode and a relatively transparent charge transport layer (CTL) are applied to mitigate optical

losses [17, 18]. A scheme of a PSC in an inverted p-i-n configuration is depicted in figure 1 (b). Indium tin oxide (ITO)-coated glass serves as fundament for the solar cell and as light-transmissive front electrode. The HTL and the ETL are providing an efficient charge transport from the intrinsic perovskite layer, which generates electron hole pairs upon illumination and the electrodes of the solar cell [19, 20]. The chemical structures of the charge transport and buffer layers employed in this thesis are displayed in figure 2. Common hole transport materials in perovskite solar cells are organic compounds like poly-bis(4-phenyl)(2,4,6-trimethylphenyl)amine (PTAA) [21–23], poly(3,4-ethylenedioxythiophene):poly-(styrenesulfonate) (PEDOT:PSS) [16, 24, 25] and the metal oxide NiO_x [15, 26, 27].
The overlying perovskite layer is very sensitive to oxygen and moisture, which both can lead to degradation of the perovskite. For blocking oxygen/moisture penetration and passivating surface defects in perovskites, an additional passivation layer can be placed on the perovskite and the ETL such as phenylethylammonium iodide (PEAI) [21, 28]. A defect-free physical contact between the ETL and the perovskite is essential for improved electron extraction [29].

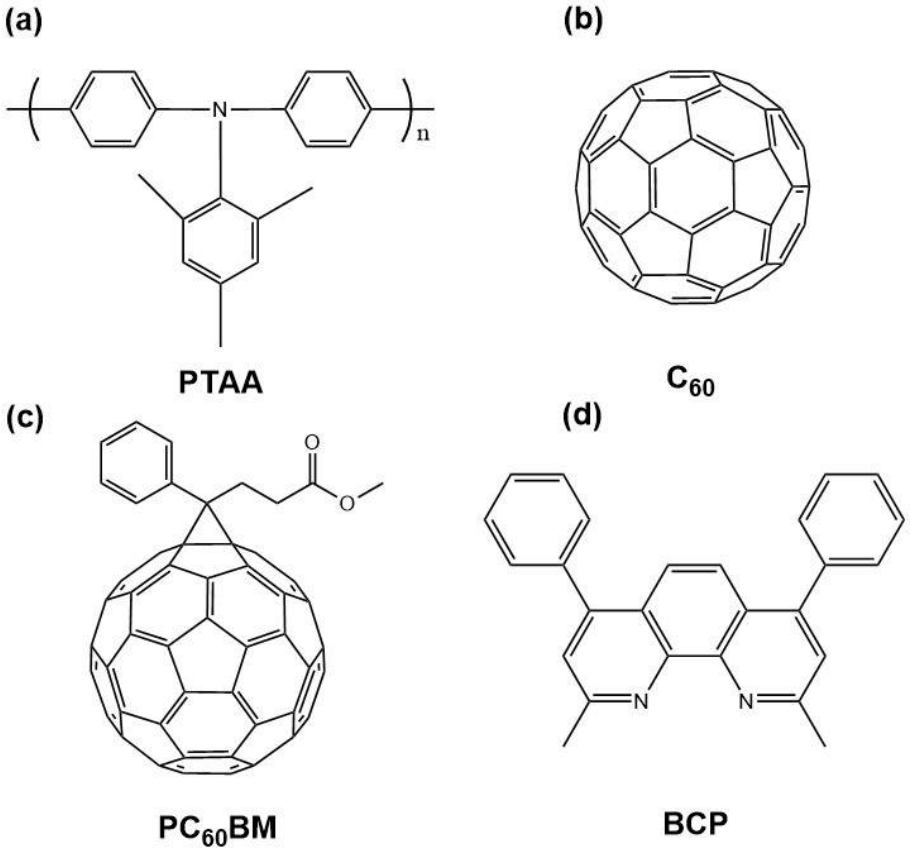

Figure 2: Chemical structures of utilized hole transport, electron transport and buffer layer materials. PTAA (a) as HTL, C_{60} (b) or $PC_{60}BM$ (c) as ETL and BCP (d) as buffer layer.

The ETL is mandatory for maintaining air stability [30] and protects the electrode material from the corrosive perovskite [31]. Organic compounds such as fullerene-C_{60} (C_{60}) [22, 23, 32] or phenyl-C_{61}-butyricacidmethylester ($PC_{60}BM$) [33–35] and the metal oxide SnO_2 [36–38] are commonly used as ETL in perovskite solar cells. Bathocuproine (BCP) can be applied as buffer layer between the organic electron transport materials C_{60} or $PC_{60}BM$ and the back-metal cathode (e.g. Ag, Al or Au) [26, 34, 39]. A buffer layer is applied between the ETL and the back-electrode in order to eliminate the interfacial charge accumulation and to increase device performance [40].

1.1.2 Energy diagrams and optoelectronic properties of layers in a perovskite solar cell

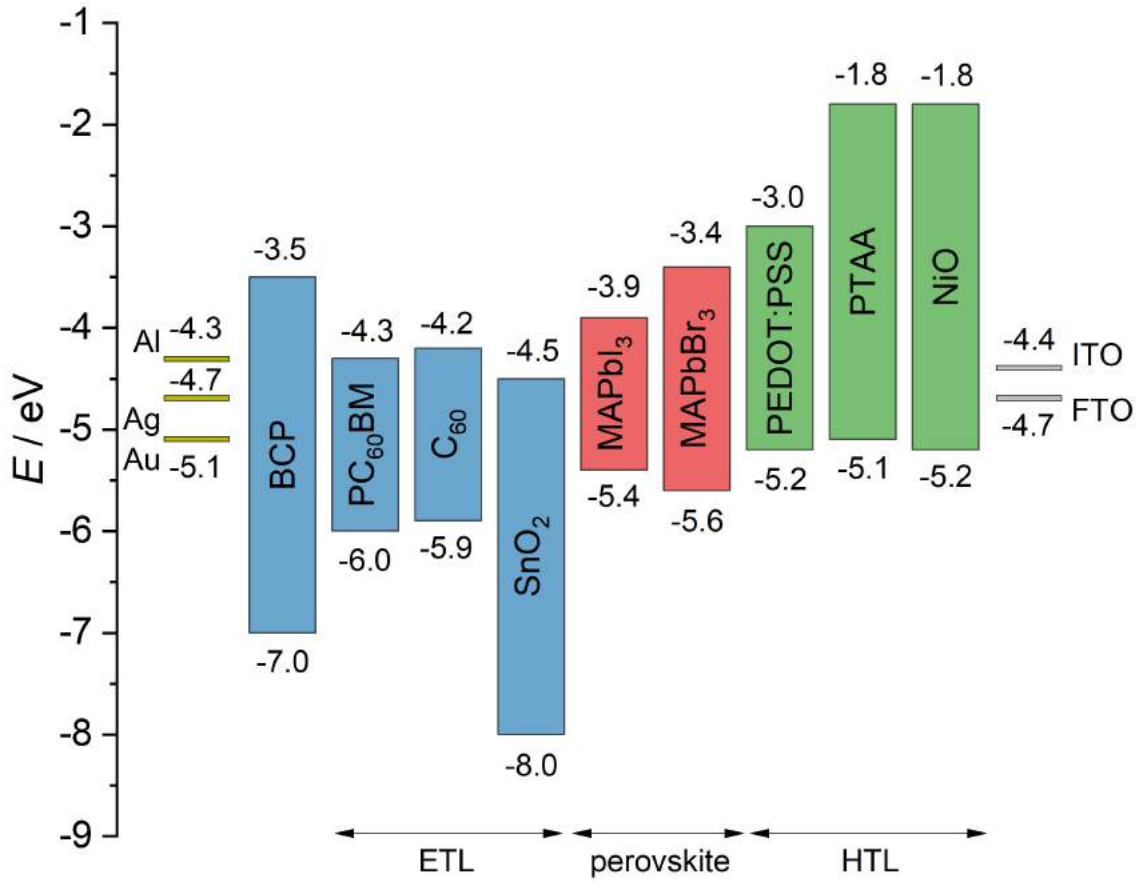

Figure 3: Energy level vs vacuum energy level diagram of frequently used electrode materials, electron transport layers, perovskites, hole transport layers and transparent conductive oxides. The lines in the diagram represent work functions, whereas the bands represent the LUMO (upper end) and HOMO (lower end) of the CTL-materials, respectively the CB and VB of the perovskites.

In figure 3 the energy level of the valence band (VB) and the conduction band (CB) for several electron transport-, perovskite- and hole transport-layers and the work

functions of electrode metals and transparent conductive oxides are visualised. The absorption of a photon in a perovskite leads to the excitation of an electron from the VB to the CB. The generated, bound electron-hole pair is called an exciton. The exciton can dissociate into charge carriers, which move over the CTLs to the electrodes. Therefore holes are transported from the VB of the perovskite to the highest occupied molecule orbital (HOMO) of the HTL and are subsequently extracted to the anode. Electrons move from the CB of the perovskite to the lowest unoccupied molecule orbital (LUMO) of the ETL and are subsequently extracted to the cathode. Because of this, the energy bands of the perovskite and the charge transport layers have to be well aligned to enable efficient charge extraction, charge transport and consequently, high power conversion efficiencies. It has to be noted that during the transport free charge carriers can be captured or nonradiatively recombined by traps and defects in the perovskite or in the charge transport layers. These phenomena lead to charge losses at interfaces as well as in the bulk, which results in overall performance impairments in a PSC. These include a loss in fill factor (*FF*), open-circuit voltage (V_{OC}) deficits, a decrease in short-circuit current density (J_{SC}) and hysteresis effects in current/voltage curves (derivation between the forward and backward scan) [19, 39, 41, 42].

1.1.3 Determination of band gap and Urbach energy via data from absorptance spectra

The optical band gap of a semiconductor with direct optical transitions is obtained by creating a Tauc plot. $(\alpha E)^2$ is plotted against photon energy E, where α stands for the absorption coefficient. The band gap is determined by extrapolating the straight-line part in the Tauc plot to the E axis and obtaining the energy value of the intersection [44, 45]. α is determined using equation 1.1, where d is the film thickness, A is the absorptance and T is the transmittance of the probe film [43, 44]:

$$\alpha = \frac{1}{d} \ln\left(1 + \frac{A}{T}\right) \tag{1.1}$$

The Urbach energy E_U and its relation to the material parameters α_0 and E_0 are described at energies below the bandgap by equation 1.2. This sub-band gap region is called the Urbach tail and is utilized for obtaining the Urbach plot [46]. It can be obtained by plotting $\ln(\alpha)$ vs. E below the band gap of the semiconductor. The reciprocal value of the slope of the function corresponds to the Urbach energy [45, 47].

$$\ln\left(\alpha(E)\right) = \ln\left(\alpha_0\right) - \frac{E_0}{E_U} + \frac{1}{E_U} E \tag{1.2}$$

1.2 Wide-band gap perovskite solar cells

In the last years wide-band gap (WBG) perovskites have received considerable attention as they can be utilized in tandem solar cells in combination with a narrow band gap solar cell or in light-emitting diodes (LED) [13, 48]. There are several definitions at which minimum E_g a PSC is declared as wide-band gap solar cell ranging from 1.60 eV - 1.70 eV [48–51]. In this thesis, WBG cells are defined as solar cells with an $E_g \geq 1.65$ eV.

The band gap of a I/Br-mixed halide perovskite can be easily modified by adjusting the bromide content of the perovskite. As an example, by raising the bromide mole fraction x from 0 to 1 in a classical $MAPb(I_{1-x}Br_x)_3$ perovskite, the E_g can be increased from 1.55 eV to 2.3 eV [22, 52]. The band gap can also be modified over changing the A-site cation stoichiometry. By increasing the Cs amount in a $FA_{1-x}Cs_xPb(I_{0.95}Br_{0.05})_3$ perovskite from x = 0.15 to x = 0.40, the E_g can be raised from 1.56 eV to 1.62 eV [53]. However, there are difficulties associated with the fabrication of WBG solar cells. One topic is the open circuit voltage deficit, which results from non-radiative recombination losses. This describes the phenomenon in WBG perovskite solar cells that with increasing band gap no increase in V_{OC} is observed and a plateau in V_{OC} is observed [19, 41, 50]. Also, perovskites with a large band gap suffer from a phase segregation into a I-rich and a pure Br-phase under illumination. This causes instability and a performance decrease in perovskite solar cells, which is a key topic in WBG perovskite research [54–57].

1.2.1 Phase segregation and open circuit deficit in perovskite solar cells with a large band gap

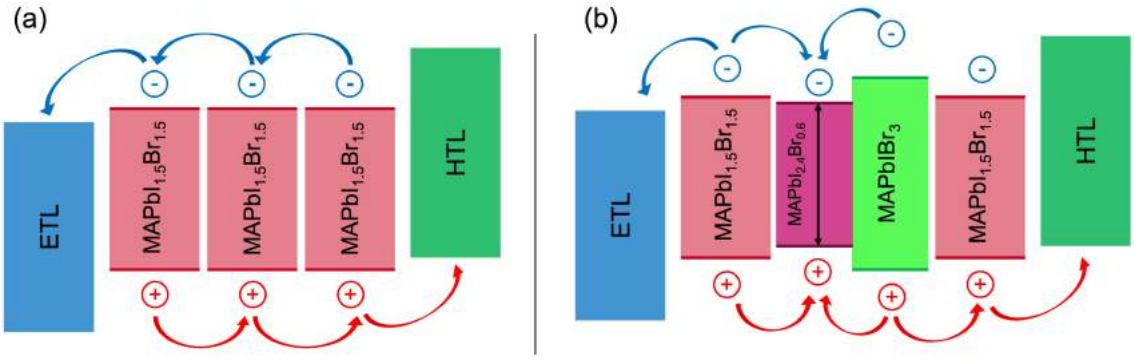

Figure 4: A proposed scheme illustrating the band alignment in a $MAPbI_{1.5}Br_{1.5}$ perovskite before (a) and after (b) illumination with light. The irradiation leads to the formation of a Br-rich and a I-rich site, where the latter one acts as charge recombination centre [57, 61, 62].

In the year 2015, *Hoke et al.* reported visible light-induced transformations in $(CH_3NH_3)Pb(I_{1-x}Br_x)_3$ perovskites [58]. The phenomenon was attributed to a halide segregation within the perovskite, which is from there on called the Hoke effect [58]. The phase segregation is fully reversible. Illuminated materials transform to their initial states after a few minutes in the dark [15, 48, 59]. Perovskites with a high concentration of bromide and a bandgap $\geq 1.70\,\text{eV}$ are prone to a photo-induced phase segregation. This typically takes place at grain boundaries and leads to phase instability [15, 51, 60]. In WBG perovskites the Hoke effect is assumed to create a high open-circuit voltage deficit V_{def}, which is defined as the fraction of E_g and the elementary charge q minus V_{OC} (equation 1.3). However, recently high V_{def} values have been attributed to PSC/CTL interfacial nonradiative recombinations and a high interfacial defect density additional to the halide segregation [48, 50].

$$V_{\text{def}} = \frac{E_g}{q} - V_{OC} \tag{1.3}$$

It is assumed that upon illumination, halide migration takes place within the bulk of the perovskite and leads to the formation I-rich and Br-rich domains (figure 4) [56, 58]. The ion migration is also responsible for a charge carrier accumulation during PSC operation and creates a hysteresis effect in current/voltage curves. From an energetic point of view the formed iodide-rich phase has a smaller E_g, a higher VB and a lower CB, than the original $AB(I_{1-x}Br_x)_3$ phase. For the bromide-rich phase the reverse effect takes place. Consequently, charge carriers are trapped in the iodide-rich domains. Trapped holes are believed to promote phase segregation [58]. Also, the charge carrier accumulation in the iodide-rich phases, which act as recombination centres, produces an additional red-shifted photoluminescence peak [49, 50, 53, 57–59, 61–63]. According to several studies, results of XRD and *PL* measurements suggest that formed iodide-rich perovskite phases have a x of ~ 0.2, independently from the original (pre-illumination) bromide mole fraction of the perovskite [58, 61, 64].

Halide segregation is detectable by X-ray diffraction (XRD, a splitting of peaks is observed), by *PL* spectroscopy (an additional red-shifted peak occurs) and by transient absorption spectroscopy (where a migration of charge carriers to I-rich phases is observed) [58, 65].

Up to date, there are three main strategies how to prevent or to reduce photo-induced phase segregation in WBG solar cells. One approach is to change the stoichiometry of the A-site cation, e.g. FA/Cs-double cation perovskites show high photostability compared to MA single-cation perovskites, especially in the region of 10 % - 30 % Cs at the A-site [66]. Cs/FA/MA triple-cation perovskites are also promising candidates

for increased stability against halide segregation [67, 68]. The second approach is to increase the crystallinity of a perovskite, e.g. by increasing the grain size of the perovskite film [69–71]. An increase of grain size and crystallinity was observed for a $MAPbBr_{0.6}I_{1.4}$ PSC by changing the HTL from PEDOT:PSS to hydrophobic PTAA [69]. *Braly et al.* reported that increasing the annealing temperature for a $FA_{0.83}Cs_{0.17}Pb(I_{0.66}Br_{0.34})_3$ layer from 75 °C to 165 °C resulted in larger grains and photostability [72]. The third approach is to reduce the trap density within the perovskite. Thin 2D passivation agents are one strategy to mitigate ion migration and to reduce trap density [21, 23, 116]. A reduced defect density through passivation was also obtained, when a potassium iodide solution was incorporated into the perovskite precursor solution [49].

1.2.2 Use of wide-band gap perovskites in tandem solar cells and other applications

Single junction solar cells are bound to the theoretical Shockley-Queisser limit, which describes a maximum possible *PCE* of slightly above 30 % [11, 12]. This limit can be bypassed by stacking 2 semiconductors with different band gap on top of each other, which results in a two-junction solar cell [73, 74]. *Steiner et al.* reported in 2021 a GaInP/GaAs tandem solar cell with a *PCE* of 32.9 % under a 1-sun AM1.5G spectrum [75]. Tandem solar cells are classified into a two-terminal (2T) and into a four-terminal (4T) design. A 2T tandem cell consists of two monolithically connected sub-cells with an intermediate recombination layer or a tunnel junction layer. The 2T solar cell requires only two external electrical contacts at the top and at the bottom. In 4T solar cells the sub-cells are produced on two separate substrates and must be connected by an external circuit, which results in four external contacts [27, 73].
Figure 5 displays a scheme of a tandem solar cell in a 2T design. The (sun-)light enters from the bottom through a transparent ITO glass substrate. The front sub-cell consists of a WBG solar cell which absorbs the high-energy photons. Low-energy photons pass the front cell and are absorbed by the rear sub-cell, which consists of a narrow band gap absorber. In order to achieve a large *PCE*, sub cells with non overlapping absorption spectra, with high external quantum efficiencies, and matched currents are required (see section 1.2.3) [34]. The recombination layer must be very thin, since it has to be transparent for photons absorbed in the rear sub-cell, and must have a low electrical resistance [35]. Typical materials utilized for recombination layers are thin metal layers, doped PEDOT:PSS, inorganic ZnO or a transparent conductive oxide such as ITO [76]. Up to date, perovskites are utilized in perovskite/Si, perovskite/$Cu(In,Ga)Se_2$ (CIGS) and in perovskite/perovskite tandem solar cells [34, 35, 37]. Perovskite/Si tandem solar cells are a promising

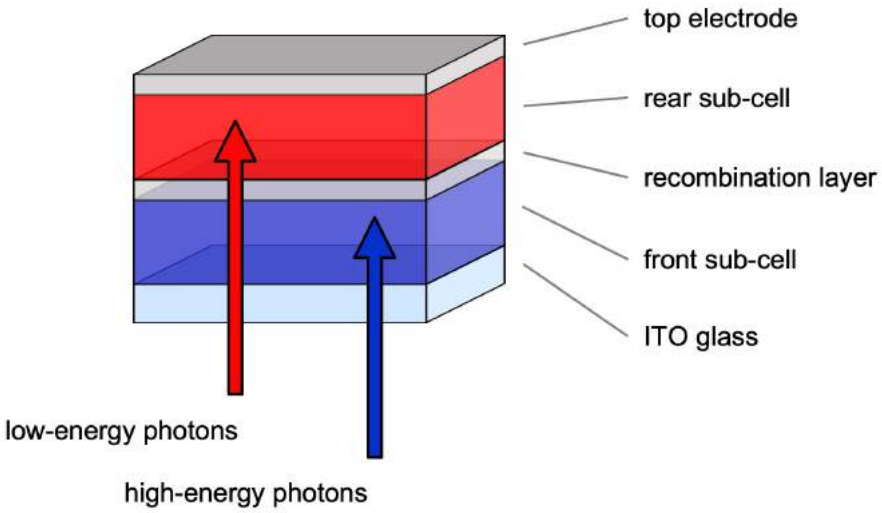

Figure 5: A tandem solar cell in a 2-terminal configuration. The wide-band gap front (bottom) sub-cell absorbs the high energy part and the narrow band-gap rear (top) sub-cell absorbs the low energy part of the incident light.

combination as Si solar cells offer a low E_g of 1.12 eV, are cheap, are produced on a large scale and offer a high stability [73, 77]. Recently, tandem solar cells, consisting of a PSC and an organic solar cell (OSC), are gaining focus in research [26, 37, 38, 78, 79]. They possess the advantage that standard solvents employed for fabrication of organic bulk heterojunction solar cells are typically nonpolar (e.g. chlorobenzene or chloroform) and do not interact with the underlying perovskite layer [79].
The possibility of tuning the bandgap of perovskites can be utilized in LEDs with a controllable output colour. The emission spectrum can be varied by adjusting the crystal size and the perovskite composition. However, perovskite LEDs strongly suffer from nonradiative recombination losses, therefore further research is required [70, 80]. Various reports for perovskite based LEDs with different colours are available. E.g. a green light LED with 20.3 % *EQE* was reported, which consists of a WBG $CsPbBr_3$ perovskite mixed with a MABr additive [81]. Also, a blue LED reaching 9.5 % was reported, where quantum-confined perovskite nanoparticles were embedded into a WBG quasi-two-dimensional perovskite [82]. Recently, the possibility of producing perovskite LEDs by inkjet printing was demonstrated, which reveals a future low-cost manufacturing method [83].

1.2.3 Current matching in two-terminal tandem solar cells

In a TSC, the photocurrent is always limited by the lower sub-cell current, which is determined by Kirchhoff's law for a connection in series. This means in a TSC the sub-cell currents must match, in order to mitigate a current loss and to improve the *PCE* [73]. Current matching calculations in tandem solar cells are complex, as

stand-alone solar sub cells perform differently in tandem solar cells due to reflections, interferences, scattering and luminescence coupling [11, 76, 84, 85]. Current matching can be optimized by adjusting the thickness of the photoactive layer of the sub-cells [73, 78]. In case of a PSC as WBG absorber, current matching can also be achieved by tuning the band gap of the perovskite.

In order to determine the optimal band gap of a narrow band gap sub-cell for a current match with a WBG sub-cell with 1.73 eV, which was the band gap of the investigated WBG perovskite in this thesis, a model of an ideal 2T tandem solar cell with no optical scattering or reflection and no luminescent coupling was used.

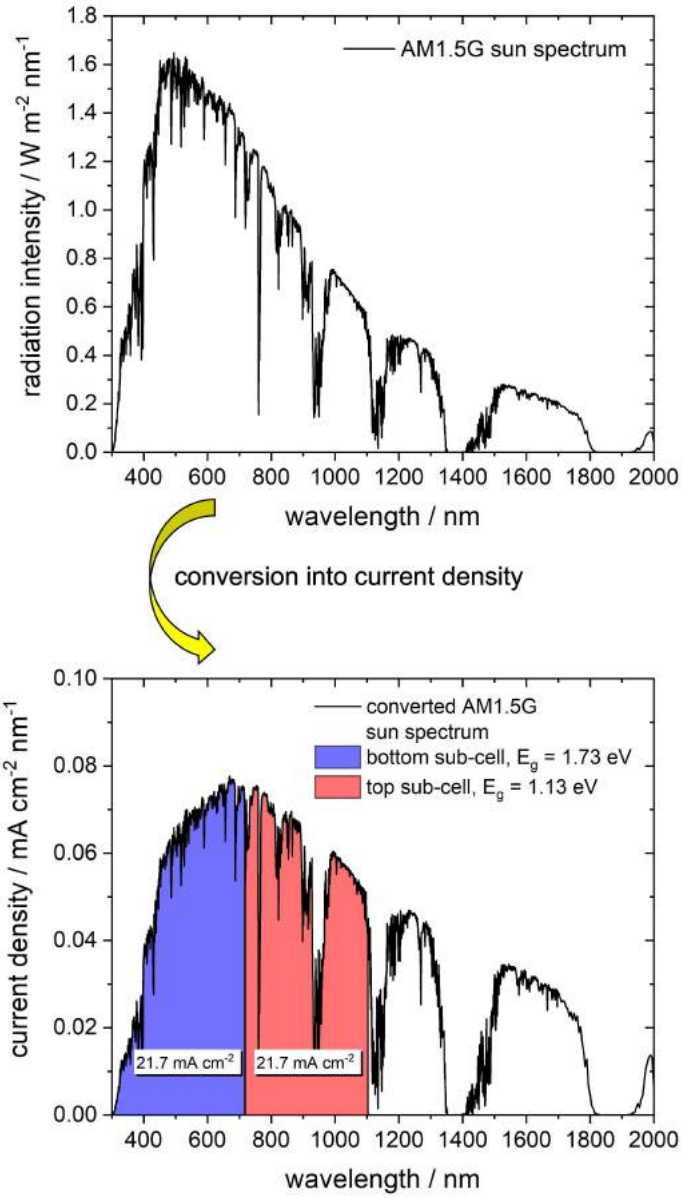

Figure 6: Current match for an ideal 2T tandem solar cell with no optical scattering or reflection and no luminescent coupling. The sun radiation intensity (AM1.5G) is converted into current density for 100 % *EQE* for the entire spectrum.

The J_{SC} can be calculated from the solar radiation intensity $\phi_{AM1.5G}$, utilizing formula 1.4. Here, q is the electron charge, h is the Planck constant, λ is the wavelength of incident light, c is the speed of the light and $A(\lambda)$ is the absorption of this absorber [86, 87]. $A(\lambda)$ is set to 1 for all wavelengths.

$$J_{SC} = q \int_{\lambda_1}^{\lambda_2} \frac{A(\lambda) * \lambda * \phi_{AM1.5G}}{h * c} d\lambda \tag{1.4}$$

The result of the conversion of solar radiation intensity to photocurrent is displayed in figure 6. A current match of bottom cell with E_g = 1.73 eV and a top cell with E_g = 1.13 eV is received. An optimal E_g of 1.14 eV for the narrow band gap cell for a 1.73 eV WBG cell is calculated with the empirical formula $E_{g(b)} = 0.64 * E_{g(t)} + 1$, which is also based on a double-junction tandem solar cell [88].
Si, with a band gap of 1.12 eV, is a suitable material for the top sub-cell [76]. The organic acceptors SiOTIC-4F and COTIC-4F with an E_g of 1.17 eV and 1.10 eV, respectively, are near the calculated optimal band gap [89]. Narrow band gap perovskites with an $E_g < 1.2$ eV are not available, as these composites suffer from instability. $FA_{0.75}Cs_{0.25}Sn_{0.5}Pb_{0.5}I_3$ with a band gap of 1.2 eV was reported as thermally and atmospherically stable [90]. However, mixed halide perovskites have the advantage of band gap tuning by varying the bromide content, making it possible to enable PSCs, beside organic solar cells, as narrow band gap solar cells in a TSC.

2 Experimental

2.1 Materials

The materials mentioned in the experimental section and their respective supplier, purity and abbreviation can be found in table 1.

Table 1: Summary of used materials, including their supplier, purity and abbreviation.

Material	Supplier	Purity / %	Abbr.
Bathocuproine	Sensient	-	BCP
Cesium bromide	Alfa Aesar	99.999	-
Cesium iodide	Alfa Aesar	99.999	-
Chlorobenzene	Sigma Aldrich	99.8	CB
Diethyl ether	Sigma Aldrich	99.5	-
Dimethyl sulfoxide	Sigma Aldrich	99.9	DMSO
Encapsulation Epoxy E131	Ossila	-	-
Ethanol	fischer scientific	$\geq$ 99.5	EtOH
Formamidinium bromide	-	-	FABr
Formamidinium iodide	-	-	FAI
Fullerene-C_{60}	Sigma Aldrich	99.9	C_{60}
Indium doped tin oxide on glass	Xinyan Hongkong	-	ITO
Isopropanol	VWR Chemicals	100	IPA
Lead(II) bromide	Sigma Aldrich	99.9999	-
Lead(II) iodide	Alfa Aesar	99.9985	-
N,N-Dimethylformamide	Sigma Aldrich	99.8	DMF
Perfluorodecalin	F2 Chemicals	-	-
Phenyl-C_{61}-butyricacidmethylester	Solenne	99	$PC_{60}BM$
Poly[bis(4-phenyl)(2,4,6-trimethylphenyl)amine (M_w 13000 g mol^{-1})	Ossila	-	PTAA
Silver	-	-	Ag
Toluene	Sigma Aldrich	99.8	-

2.1.1 Preparation of double-cation perovskite precursor solution

The $FA_{0.8}Cs_{0.2}Pb(I_{0.7}Br_{0.3})_3$ precursor was prepared in an inert glovebox filled with nitrogen ($H_2O < 0.1$ ppm and $O_2 < 5.0$ ppm). The components FAI (148.6 mg, 864.1 µmol), PbI_2 (273.8 mg, 593.9 µmol), $PbBr_2$ (178.4 mg, 486.1 µmol) and, CsI (56.2 mg, 216.3 µmol) were dissolved with an 1 mL solvent mixture of DMF and DMSO (volumetric ratio 9:1). The resulting 1.08 M $FA_{0.8}Cs_{0.2}Pb(I_{0.7}Br_{0.3})_3$ precursor solution was stirred vigorously over night at room temperature. It has to be noted that the DMF/DMSO ratio has a significant impact on the solubility and on the crystallization

rate of perovskite precursor, as DMSO has a larger coordination strength to PbI_2 than DMF [91, 92]. Prior to the spin coating, the stirring temperature was increased to 65 °C for 60 min in order to increase the solubility of the perovskite precursor. After this step, the precursor solution was cooled to room temperature and filtered through a 0.45 µm polytetrafluoroethylene (PTFE) syringe filter.

Table 2: Masses and amounts of materials for the preparation of perovskite precursors with varying bromide content for 1 mL solvent.

material	0 % Bromide		30 % Bromide		40 % Bromide		50 % Bromide	
	mass / mg	amount / µmol	mass / mg	amount / µmol	mass / mg	amount / µmol	mass / mg	amount / µmol
FAI	148.6	864.1	148.6	864.1	148.6	864.1	148.6	864.1
PbI_2	497.9	1079	273.8	593.9	199.1	431.9	124.4	269.9
$PbBr_2$	0	0	178.4	486.1	237.9	648.1	297.3	810.1
CsI	56.2	216.3	56.2	216.3	56.2	216.3	56.2	216.3

2.1.2 Preparation of triple-cation perovskite precursor solution

The $Cs_{0.1}(FA_{0.6}MA_{0.4})_{0.9}Pb(I_{0.6}Br_{0.4})_3$ precursor was prepared under inert conditions. According to table 3, FAI (206.6 mg, 1201.4 µmol), PbI_2 (613.2 mg, 1339.1 µmol), MABr (89.4 mg, 799.2 µmol) and $PbBr_2$ (293.3 mg, 798.4 µmol) were dissolved in 1.2 mL mixture of DMF/DMSO (4:1 for batch 8 and 5:1 for batch 9). Additionally to this, a stock solution containing CsI (259.6 mg, 999.2 µmol) and PbI_2 (462.3 mg, 1002.8 µmol) in 1 mL DMSO (batch 8) or 833 µL DMF and 1167 µL DMSO (batch 9) was prepared. The stock solutions were stirred for 1.5 h at 60 °C and were then added to the perovskite precursor solution (120 µL stock solution for batch 8 and 240 µL for batch 9). The solution was subsequently stirred at 60 °C over night. Prior to the spin coating of the solution, it was cooled to room temperature and filtered through a 0.45 µm PTFE syringe filter.

Table 3: Masses and amounts of materials for the preparation of a triple-cation perovskite precursor for 1.2 mL solvent.

material	mass / mg	amount / µmol
FAI	206.6	1201.4
PbI_2	613.2	1330.1
MABr	89.4	799.2
$PbBr_2$	293.3	798.4

2.1.3 Preparation of perovskite precursor solutions with varying bromide content

The influence of the bromide content x between 0 and 0.5 in the perovskite precursor $FA_{0.8}Cs_{0.2}Pb(I_{1-x}Br_x)_3$ onto the band gap of the semiconductor was examined. For this, solutions with bromide contents of 0 %, 40 % and 50 % were prepared according to table 2. The bromide and iodide ratio was modulated by variation of PbI_2 and $PbBr_2$ content, enabling a theoretical maximum bromide content of 66.67 % with the used substances. Preparation of the precursor solutions was carried out as in 2.1.1, including the filtration of the prepared salt solutions. In order to obtain mixtures with 10, 20 and 30 % bromide contents, the prepared 0 % Br and 40 % Br solutions were mixed with a volumetric ratio of 3:1, 2:2 and 1:3, respectively.

2.2 Perovskite solar cell fabrication

ITO-coated glass (25.9 mm $\times$ 25.9 mm) served as fundament for the deposition of the functional layers of the perovskite solar cell. A central ITO stripe was prepared by protecting the ITO layer with a polyvinyl chloride (PVC) tape. The uncovered ITO was etched away by immersing the ITO-coated glass in concentrated hydrochloric acid (HCl, 37 wt% in H_2O) for 5 min. This served to prevent the chance of short circuits between the silver top contacts and the ITO back contact in a PSC. The ITO glass was cut to a size of 25.9 mm $\times$ 25.9 mm with a glass cutting tool. The ITO glasses were cleaned with toluene and soft wipes. The substrates were further cleaned in a sonification bath in Hellmanex solution (2 vol% in H_2O) at 80 °C, in acetone at room temperature and in isopropanol at room temperature, for 30 min each. Between sonification in Hellmanex solution and acetone, the substrates were immersed into deionized water two times.

Directly before the deposition of the respective layers of the perovskite solar cell, the cleaned ITO-glass substrates were treated with an O_2 plasma for 10 min. The films were prepared in nitrogen atmosphere ($H_2O < 0.1$ ppm and $O_2 < 5.0$ ppm). For the deposition of a thin PTAA film, which served as hole transport layer, a 1.5 mg mL^{-1} solution of PTAA in isopropanol (mixture was stirred over night at room temperature) was spin coated onto the ITO substrate with the parameters listed in table 4. Promptly after PTAA deposition, the substrates were annealed on a hot plate at 100 °C for 10 min. After approximately 5 min, the samples were taken from the hot plate and patterned on the ITO covered edges with a toluene-soaked cotton pad.

Figure 7: 8 completed perovskite solar cells consisting of (from bottom to top: An ITO-glass, a PTAA hole transport layer, a wide-band gap perovskite layer, a C_{60} electron transport layer, a BCP buffer layer and Ag electrode contacts.

Onto the PTAA film, a perovskite film was grown by spin coating with the parameters listed in table 4. A freshly filtered perovskite precursor solution was used, which was produced as described in section 2.1.1 and 2.1.2. For the double-cation perovskite 35 s before the end of the spin coating program, an antisolvent was drop casted onto the substrate. For the double cation recipe, two solvents, diethyl ether and toluene, were investigated as antisolvent. In the case of diethyl ether as antisolvent, 750 µL of liquid were drop casted by hand using a pasteur pipette over a range of of 3 s with a close distance and a careful back and forth movement onto the substrate. In the case of toluene as antisolvent, an antisolvent pump was used for application of the toluene. For the triple-cation perovskites, chlorobenzene was applied with the antisolvent pump (see table 4). The antisolvent pump consisted of a single-use 1 mL syringe, a pump connected to the syringe and a small display for entering settings. The setup drops the antisolvent onto the substrate with precise settings and therefore, it enables higher reproducibility of the PSC production. 150 µL toluene were applied from 3 mm distance onto the centre of the rotating substrate within 1 s. In the moment of antisolvent drop casting, the perovskite film turned from yellowish to light brown. Promptly, after the end of the spin coating program, the substrates were annealed at 65 °C for 2 min and at 100 °C for 10 min (100 °C for 30 min as second step for batch 9). During the annealing process, the color of films changes from light brown to dark brown. After 5 min at 100 °C, the substrates were patterned with DMF as described before for the PTAA layer.

Either C_{60} or $PC_{60}BM$ were used as electron transport layer. 20 nm of C_{60} were evaporated onto the perovskite film by physical vapor deposition (PVD, Vaksis PVD–handy) with a evaporation rate between 0.2 Å s^{-1} and 0.5 Å s^{-1} at a pressure of $2 * 10^{-6}$ mbar in the first variant. For $PC_{60}BM$ deposition, a 20 mg mL^{-1} solution in chlorobenzene

(mixture was stirred over night at room temperature) was spin coated onto the perovskite substrate under inert conditions with the parameters listed in table 4. For both materials, BCP was used as buffer layer between the silver electrode and the ETL to enhance the cell performance [93]. According to the parameters in table 4, a 0.5 mg mL^{-1} solution of BCP in isopropanol was spin coated onto the substrates. The cells were patterned with isopropanol as described before for the PTAA layer, without annealing.

Ag was used as electrode material for the working electrode contacts for the perovskite sub-cells and as counter electrode contact to the underlying ITO layer. 100 nm of Ag were deposited with a rate of 0.2 Å s^{-1} and 1.4 Å s^{-1} onto the substrates by PVD (UNIVEX 350, Leybold) using a mask, which forms the silver structure observable in figure 7. The yielded device consists of 8 perovskite solar cells, 2 counter electrode contacts and was stored under inert conditions in a glove box. ($H_2O < 0.1$ ppm and $O_2 < 0.1$ ppm).

Table 4: Parameters for the preperation of thin films on a spin coater.

material	speed / rpm	time / s	acceleration / rpm s^{-1}
PTAA	6000	30	2000
DMF	4000	10	2000
double-cation perovskite	480	2	480
	4000	[a]60	2000
triple-cation perovskite	4980	[b]30	2490
PC60BM	1320	16	660
	1980	15	990
BCP	4980	30	2490

For the fabrication of a perovskite thin film (a) 35 s and (b) 8 s before the end of the spin coating program, antisolvent was dropcasted onto the substrate.

2.2.1 Fabrication of perovskite films with varying bromide content for analysis

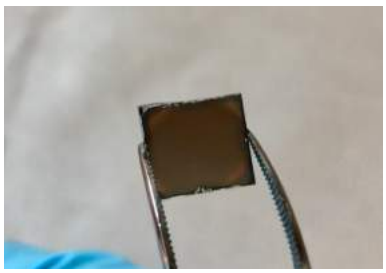

Figure 8: Double-cation perovskite film on quartz glass with the composition $FA_{0.8}Cs_{0.2}Pb(I_{0.6}Br_{0.4})_3$ processed by spin coating.

Perovskite films with bromide contents ranging from 0 % to 50 % were processed on PTAA coated quartz glass (10 mm × 10 mm) with precursor solutions prepared the same as in section 2.1.3 and with the parameters listed in table 4. The cleaning of the glass substrates, the processing of the PTAA solution and the perovskite solution were carried out according to the procedure in 2.2. However, the following adaptations have been made: Neither the PTAA film, nor the perovskite film were patterned. 40 µL toluene were dropped onto the substrate within 0.25 s. A perovskite sample with 40 % Br prepared according to the instruction above can be seen in figure 8.

2.3 Encapsulation of solar cells

In order to protect the solar cells from oxygen- and moisture-induced degradation, a glass slide (17.5 mm × 17.5 mm) was glued on the cell with an epoxy resin (Encapsulation Epoxy E131, Ossila). The resin was cured through irradiation with UV light 3 times for 3 min each.

2.4 External quantum efficiency measurement

The *EQE* of a solar cell was measured with the following setup: Light of a Xe-lamp was modulated through a chopper (173 Hz) and filtered with a monochromator. The beam irradiated the encapsulated PSC. A lock-in amplifier (Stanford Research Systems SR830) and a potentiostat (Jaissle 1002 T-NC) processed the signal. Calibration was made with Si diode (S2281, Hamamatsu Photonics).

In order to convert the measured signal of the perovskite S_{Per} into the spectral responsivity R_{Per} (unit $\mathrm{A\,W^{-1}}$), which is required for the calculation of the *EQE*, it has to be set into an correlation to the signal of a Si diode S_{Si} and its corresponding responsivity R_{Si} from the literature [94]:

$$\frac{S_{\mathrm{Si}}}{R_{\mathrm{Si}}} = \frac{S_{\mathrm{Per}}}{R_{\mathrm{Per}}} \tag{2.1}$$

From equation 2.1, R_{Per} is determined and is used for the calculation of the *EQE*, which is apparent in equation 2.2. Here, h is the Planck constant and c is the speed of light in vacuum [95]:

$$EQE = R_{\mathrm{Per}} \times \frac{h\,c}{\lambda\,e} \tag{2.2}$$

The *EQE* is defined as the ratio of the number of charge carriers extracted under short circuit condition by a solar cell to the number of incident photons. It can also be expressed as the solar cell photocurrent $I_{ph}(\lambda)$ at a wavelength λ divided by the incident photon flow $\psi_{ph,\lambda}$ and the elementary charge *e*, as observable in equation 2.3 [96].

$$EQE(\lambda) = \frac{I_{\mathrm{ph}}(\lambda)}{\psi_{ph,\lambda}\, e} \tag{2.3}$$

2.5 Photoluminescence and electroluminescence measurements

For *PL* measurements, an encapsulated ITO/PTAA/perovskite/$PC_{60}BM$/BCP/Ag substrate was illuminated with a laser (Coherent Obis, 532 nm wavelength, 5 mW power). Quarz glass/PTAA/perovskite samples were illuminated with a 488 nm laser (Coherent Obis, 5 mW power). Quarz glass/PTAA/perovskite samples were stored in a transparent vacuum chamber (pressure $< 10^{-6}$ Pa). The emission light was directed through 2 long-pass filters (550 nm and 570 nm). A monochromator (Shamrock 303i, Andor Technology) in connection to a charge-coupled device (CCD) camera (iDus 420, Andor Technology) served as detector for the emitted light.

For *EL* measurements, charge carriers were injected into the solar cell with a source measure unit (Keithley 2401). As for the *PL* measurements, the emitted light was directed through 2 long pass filters and a monochromator. The signal was detected with a CCD.

2.6 Current/voltage measurements

For current-voltage measurements, perovskite solar cells were irradiated with a solar simulator, which imitated the AM1.5G spectrum. The emitted light intensity of the xenon lamp was calibrated with a silicon solar radiation sensor (Si-01TC, Mencke & Tegtmeyer, 0 V - 1.4 V $\widehat{=}$ 0 - 1400 W m^{-2}). The PSC was connected to a source measure unit (Keithley 2400-LV). The forward and backward scan were performed between -0.5 V and 1.5 V, the step size was 0.05 V and the measurement delay was 0.1 s.

2.7 UV-VIS spectroscopy

The transmittance of the perovskite/PTAA/quartz glass substrates was measured with a Lambda 1050 UV/Vis/NIR spectrometer (Perkin Elmer). The data interval was

chosen between 200 nm - 1100 nm. The spectrometer included a photomultiplier tube (PMT), an InGaAs detector and a PbS detector for signal processing.

2.8 Photothermal deflection spectroscopy

PDS is a highly sensitive absorptance measurement method, which allows accurate determination of the absorption coefficient of perovskites [45, 97]. The interaction of light with a thin solid film can be mainly described by three physical phenomena: Transmittance, absorptance and reflectance. However, depending on the roughness of the film, scattering can also play an important role [47]. Standard methods for absorptance determination, such as UV-VIS spectroscopy, suffer from a loss in accuracy when investigating rough films with low surface quality [98]. PDS measurements are not affected by light scattering, which makes it a powerful tool for analysis of rough materials.
Photothermal deflections measurements were performed by Konstantin Siegel and DI Felix Mayr (Johannes Kepler University Linz). The slightly modified graphs figure 9 and figure 10 are printed in this thesis with their permission. The used PDS setup consisted of a wavelength-tuneable pump laser, a probe laser, a signal detector and data acquisition instruments. The deflection of the probe beam is dependent on the pump light wavelength and the sample characteristics. The signal can be transformed into an absorptance spectrum. Detailed information on the design and calibration of the PDS setup, the measurement method and the determination of the absorptance spectrum can be found in [45].
The perovskite samples with varying bromide content as prepared in section 2.2.1 were fixed in a sample holder, which is located in an optical glass cuvette (Hellma OS) filled with perfluorodecalin. In order to obtain absolute absorptance values from PDS data, deflection measurements were scaled to absorptance values obtained from an UV/VIS spectrometer in a wavelength region of high absorption.

2.9 Scanning electron microscopy

Perovskite/PTAA films on ITO-glass and quartz glass were analysed by scanning electron microscopy (SEM) with an acceleration voltage of 7 keV. The designation of the device is JEOL JSM-6360 LV microscope and it is equipped with a Bruker Nano X-Flash detector.

3 Results and discussion

The aim of this thesis was to develop a processable and efficient perovskite solar cell with a large band gap. A perovskite solar cell based on a double-cation, mixed-halide perovskite recipe with a band gap of 1.73 eV was created and developed for following reasons: It is compatible with a 1.13 eV sub cell as this configuration shows a current match in a tandem cell as stated in section 1.2.3. According my own observations in PDS and *PL* spectroscopy, beginning at a band gap of $\sim$1.7 eV, a transition from photo-stable into photo-unstable perovskites occurs. This phenomenon is caused by light-induced phase segregation. The largest possible, stable band gap for the investigated recipe is therefore limited by the value of $\sim$1.7 eV. However, the bandgap of the double-halide perovskite can be straightly increased by increasing bromide content in the halides, which makes it a highly attractive choice for a sub cell in tandem solar cells [6, 33, 80, 99]. For this, the influence of the bromide content in a mixed-halide precursor onto the band gap was investigated by PDS and *PL* spectroscopy. The precursor composition with 30 % Br was utilized in a solar cell and the PSC was optimized for high power conversion efficiency and high open circuit voltage.

3.1 Investigation of the effect of bromide content in perovskites onto the band gap and photo stability

3.1.1 Photothermal deflection spectroscopy analysis

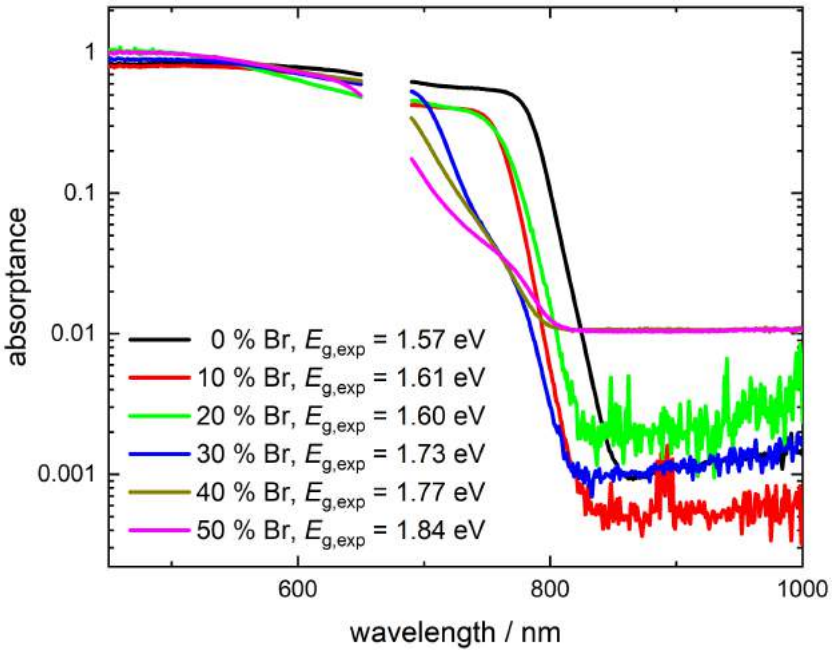

Figure 9: The effect of bromide content in a $FA_{0.8}Cs_{0.2}Pb(I_{1-x}Br_x)_3$ perovskite precursor on absorptance spectra and determinated band gaps. Quartz glass/PTAA/perovskite films were analysed by PDS.

The absorptance spectrum (figure 9) and the Urbach plot (figure 10) show the effect of bromide content variations of $FA_{0.8}Cs_{0.2}Pb(I_{1-x}Br_x)_3$ perovskites. As illustrated in figure 9, the absorptance spectra shift towards the near infrared (NIR) region with decreasing bromide fraction. At wavelengths from 761 nm to 777 nm, perovskites with 30 % to 50 % bromide content show a curvature, which is not observed for lower bromide contents. Between 650 nm and 690 nm no signal was detected due to the pump laser setup [45].

With the method shown in section 1.1.3, the experimental band gaps $E_{g,exp}$ of the perovskite samples were determined. The band gap of perovskites increases with increasing bromide content. One strong deviation from the literature values [52, 53] was observed with x of 0.2, as shown in table 5. Furthermore, the received band gaps were compared to theoretical band gaps $E_{g,lit1}$ of a $MAPb(I_{1-x}Br_x)_3$ perovskite from literature [52], where MA is used as cation. Additionally, data from [53], where a $FA_{0.8}Cs_{0.2}Pb(I_{1-x}Br_x)_3$ was investigated, was added. For the latter perovskite the $E_{g,lit2}$ values were obtained by creating a second order polynomial fit and by inter- and extra-polating data for x from 0 - 0.5 (original data for x = 0.05 - 0.3). Here, a

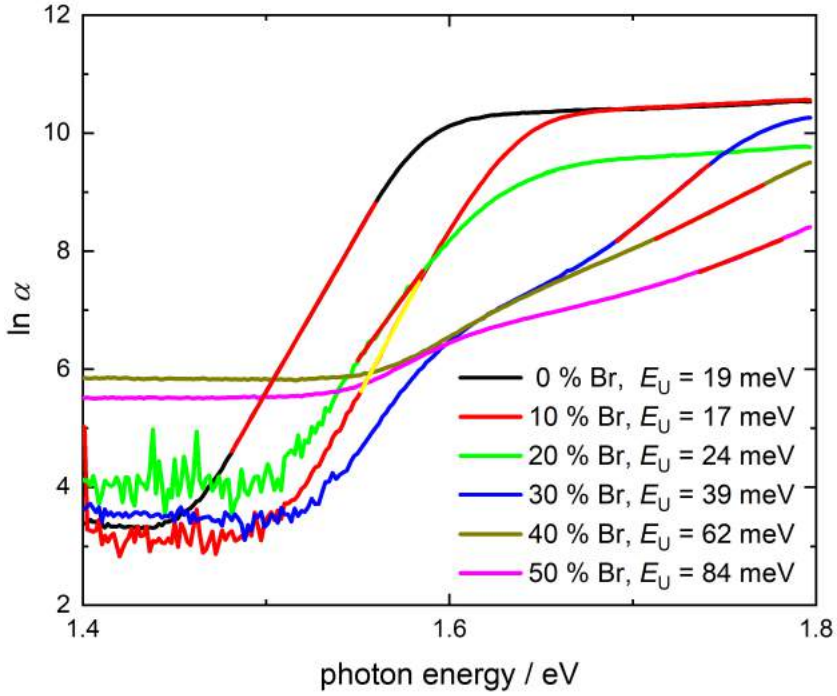

Figure 10: Urbach plot for a $FA_{0.8}Cs_{0.2}Pb(I_{1-x}Br_x)_3$ perovskite precursor with varying bromide content x. The Urbach energy is determined by a tangent through the Urbach tail.

strong correlation to the literature data for x = 0 - 0.1 and 0.3 - 0.5 exists, with a maximum deviation of 0.01 eV between $E_{g,exp}$ and $E_{g,lit1}$ [52] and 0.02 eV for $E_{g,lit2}$ [53].

Table 5: Effect of bromide mole fraction x in the perovskite onto the band gap $E_{g,exp}$, $E_{g,lit1}$ and $E_{g,lit2}$.

x	$E_{g,exp}$ / eV	$E_{g,lit1}$[52] / eV	$E_{g,lit2}$[53] / eV
0	1.57	1.57	1.55
0.1	1.61	1.61	1.61
0.2	1.60	1.66	1.67
0.3	1.73	1.72	1.72
0.4	1.77	1.78	1.77
0.5	1.84	1.85	1.82

Figure 10 shows the Urbach plot for the perovskite films with changing bromide content. The Urbach energy E_U was calculated from the sub-band gap tails as described in section 1.1.3. A general rise in Urbach energy from 19 meV at 0 % bromide to 84 meV at 50 % bromide is apparent. Low E_U values for perovskites are desirable, as this implies a low degree of structural disorder and high crystallinity [97]. $MAPbI_3$ thin films (E_g = 1.57 eV) typically have Urbach energies as low as 15 meV

[97] and the WBG perovskite $CsPb_{0.75}Sn_{0.25}IBr_2$ (E_g = 1.78 eV) as high as 47 meV [100]. Commercial semiconductors such as GaAs and crystalline Si have E_U values of 7.5 meV and 9.6 meV, respectively [41]. Perovskite thin films that were fabricated in this thesis, with 0 % bromide to 20 %, show comparable Urbach energies compared to [97]. Films with 30 % Br and above may show some structural disorder.

3.1.2 Photoluminescence analysis

In order to obtain more information about the perovskite thin films analysed in section 3.1.1, photoluminescence spectroscopy was conducted. The samples were investigated under vacuum and under atmospheric conditions at two different spots on the substrate, the normalised spectra are shown in figure 11. As expected from the absorption spectra with increasing bromide content a general shift towards higher energies was observed. It was notable that films with 0 % - 20 % Br showed only a single photoluminescence peak, whereas concentrations $\geq$ 30 % showed at least two *PL* peaks. This type of radiative recombination is an indication for phase segregation in mixed halide wide bandgap perovskites ($\geq$ 1.65 eV), which has been reported in literature [15, 48–51, 59]. The *PL* peak wavelengths of 0, 10 and 20 % Br under vacuum with 793, 771 and 775 nm, respectively, showed a good compliance with the experimental band gaps of 790, 770 and 775 nm. The *PL* spectra with higher Br concentrations exhibited a red shift compared to the absorptance spectra and showed 2 peaks per sample. The red-shifted peaks of 30 % - 50 % Br thin films measured under vacuum were within $\sim$ 769 nm - 773 nm, which correlated with the 10 % Br signal at 771 nm. This is an indication for the presence of an iodide-rich phase for perovskite samples $\geq$ 30 % Br. Figure 17 reveals that the wavlength of the curvatures that were apparent in absorptance spectra for films with $\geq$ 30 % Br, lied within in the two peaks observed in photoluminescence measurements.
Trap assisted recombinations, also called Shockley-Read-Hall recombinations, are dominant processes in perovskites and are caused by impurities and crystal disorder. They are usually non radiative and are therefore not suggested to create a shift in *PL* spectra [101–105].

When comparing the *PL* spectra under vacuum to the *PL* spectra recorded at atmospheric conditions and at two different spots, only small differences in peak shape were observed for concentrations of 30 % - 50 % Br. Figure 18 illustrates the *PL* difference at the start of illumination and after 120 s of illumination. Here also, small peak shape differences were observed for 30 % - 50 % Br films.

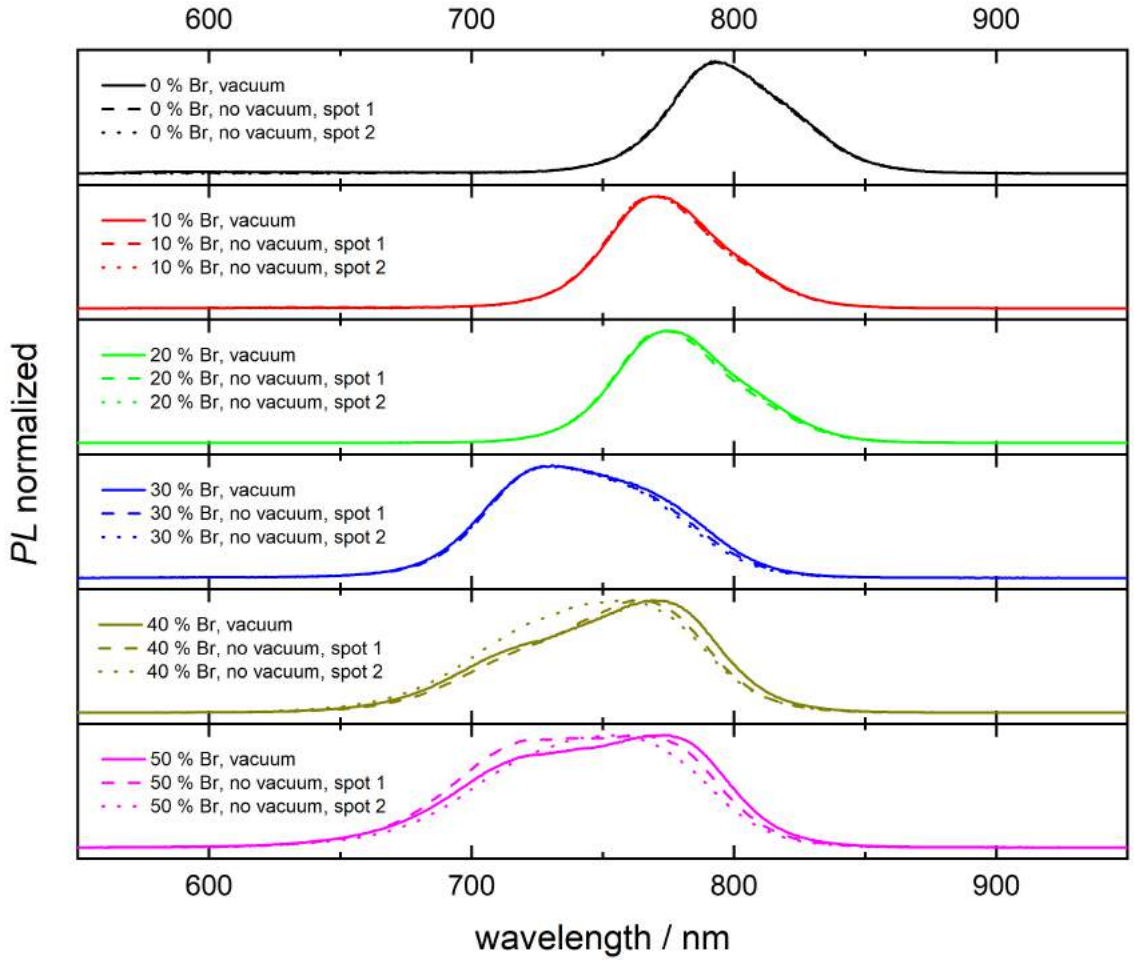

Figure 11: *PL* analysis of $FA_{0.8}Cs_{0.2}Pb(I_{1-x}Br_x)_3$ thin films with varying bromide mole fraction x. The spectra were measured under vacuum and under atmospheric conditions at two different spots. The signals were recorded with slit widths of 250 µm - 1000 µm and exposure times of 0.5 s - 1 s.

3.2 Perovskite solar cell with a large band gap

3.2.1 Fabrication of a perovskite solar cell with a large band gap

The motivation for this thesis is to create a processable and efficient perovskite solar cell with a wide band gap. Therefore, to a large extend a PSC manufacturing procedure containing a $FA_{0.8}Cs_{0.2}Pb(I_{0.7}Br_{0.3})_3$ perovskite was implemented, developed and optimized.

Figure 12 (a) and (b) illustrate the performance per produced batch solar cells in the form of percentage of solar cells working, the *PCE*, the *FF*, the V_{OC} and the J_{SC}. On the top x-axes the cumulative number cells corresponding the batches are viewable. The double-cation perovskite $(FA_{0.8}Cs_{0.2}Pb(I_{0.7}Br_{0.3})_3)/C_{60}$ cells were produced in batch 1 - 7 and 10, triple-cation perovskite $(Cs_{0.1}(FA_{0.6}MA_{0.4})_{0.9}Pb(I_{0.6}Br_{0.4})_3)/C_{60}$ cells in batch 8 - 9 and the double-cation perovskite/$PC_{60}BM$ cells in batch 11. A total

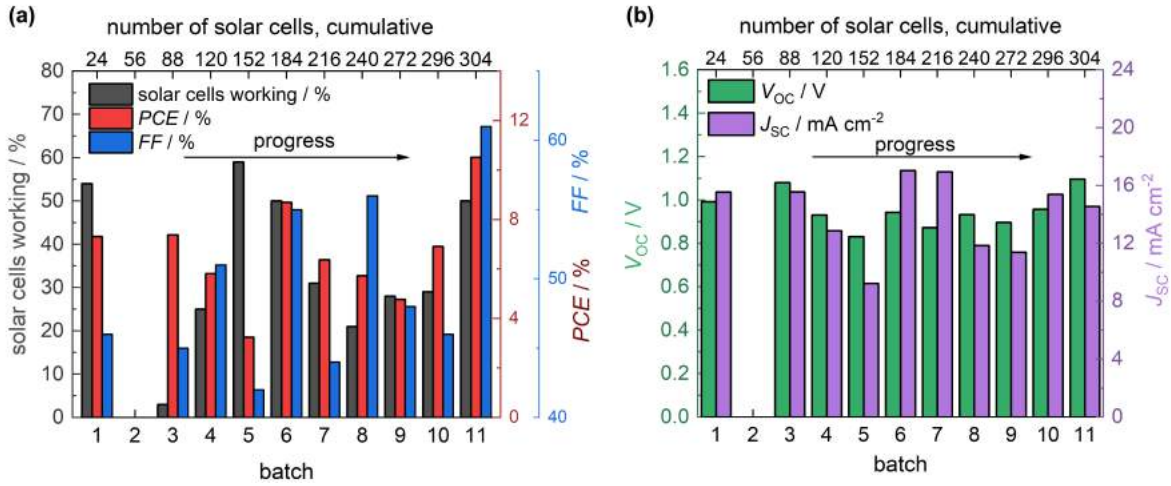

Figure 12: (a) Number of solar cells working, the *PCE*, the *FF*, (b) the V_{OC} and the J_{SC} per produced batch of perovskite solar cells. The cumulative number of solar cells is shown on the top x axes.

number of 304 solar cells were produced. From batch 7 to 10 the percentage of working solar cells was as low as 21 % - 31 %. It is assumed that during this period contamination of the glove box, such as chlorobenzene fumes, caused disturbances in the PSC manufacturing process (bad perovskite wetting behaviour and crystallisation of the perovskite before the addition of antisolvent). This observation points out the absolute necessity of cleanliness in the glove box. It is apparent that with the last batch containing 8 double-cation perovskite/$PC_{60}BM$ cells, the number of solar cells working increased to 50 %. The best *FF* with 61 %, the best *PCE* with 10.5 %, and the best V_{OC} with 1.10 V was achieved.

Following general improvements were implemented during the progress of this work:

- A special heating -, stirring- and filtration- and coating-procedure for the perovskite precursor solution (see 2.1.1) was implemented to ensure a particle free solution for solar cell production and to decrease the number of defects.
- PTAA solution concentration was decreased from 4 mg mL^{-1} to 1.5 mg mL^{-1}, as it was reported to be the optimum concentration for reaching a high *FF* and a high V_{OC} [20].
- It was ensured that no solvents were used and no waste was stored in the glovebox at least 12 hours before the start of solar cell production.
- An antisolvent pump was implemented to replace manual antisolvent dropping by a pipette, in order to increase reproducibility of the method.

- The antisolvent diethyl ether was replaced by toluene, as the latter creates perovskites with a smooth surface regardless of fast or slow antisolvent application [106].
- A DMF/DMSO mixture served as solvent for the perovskite precursor. The initial DMF/DMSO ratio was changed from 7:3 to 9:1, as DMSO has a large coordination strength to PbI_2 and therefore increases the solubility of this compound. However to high amounts of DMSO reduce crystallization rate of perovskite precursor and can lead to irregular perovskite crystals [91, 92].
- All manufacturing steps, starting from the O_2 plasma treatment of the ITO substrates to evaporation of the Ag pins, were made without disruption on one day in order to mitigate potential error sources.

3.2.2 Current/voltage measurements

In figure 13 (a) the current/voltage curves of PSCs with a $FA_{0.8}Cs_{0.2}Pb(I_{0.7}Br_{0.3})_3$ double-cation perovskite (band gap = 1.73 eV) and a $Cs_{0.1}(FA_{0.6}MA_{0.4})_{0.9}Pb(I_{0.6}Br_{0.4})_3$ triple-cation perovskite (band gap = 1.74 eV [34]) with C_{60} as ETL are illustrated. Additionally, the data of an improved $FA_{0.8}Cs_{0.2}Pb(I_{0.7}Br_{0.3})_3$ cell with $PC_{60}BM$ as ETL is shown.
It was notable that the double-cation perovskite with $PC_{60}BM$ as ETL had a 0.16 V higher V_{OC} than the combination with C_{60} (see table 6). This implied that the first combination had a lower open-circuit voltage deficit due to a lower degree of phase segregation and less surface traps [19, 21]. The PSC with the $FA_{0.8}Cs_{0.2}Pb(I_{0.7}Br_{0.3})_3$/ $PC_{60}BM$ combination had the best fill factor and the highest power conversion efficiency with 58 % - 61 % and 10.0 % - 10.5 %, respectively. Also, the corresponding current density-voltage (*JV*) curve showed a smaller hysteresis effect compared to the other two perovskite/ETL combinations. This implied that there were less interfacial trap sites, was less ion migration and polarization in this configuration [8, 27, 39, 59]. However after 10 min continuos illumination with a xenon arc lamp, the *PCE* of the champion-device decreased to 5.6 %, which is an indication for the Hoke effect (figure 19, the measurements were performed by DI^{in} Katarina Gugujonović, Johannes Kepler University Linz, for the PSC after 4 months storage in inert atmosphere). The PSC with $FA_{0.8}Cs_{0.2}Pb(I_{0.7}Br_{0.3})_3/C_{60}$ had a remarkable J_{SC} of 16.1 mA cm^{-2} - 17.0 mA cm^{-2}, which is comparable to an identical combination of perovskite and ETL with 19.0 mA cm^{-2} in literature [21]. The $Cs_{0.1}(FA_{0.6}MA_{0.4})_{0.9}Pb(I_{0.6}Br_{0.4})_3/C_{60}$ composition had a lower V_{OC}, J_{SC}, *FF* and *PCE* compared to the other compositions, which shows that this recipe needs optimisation.

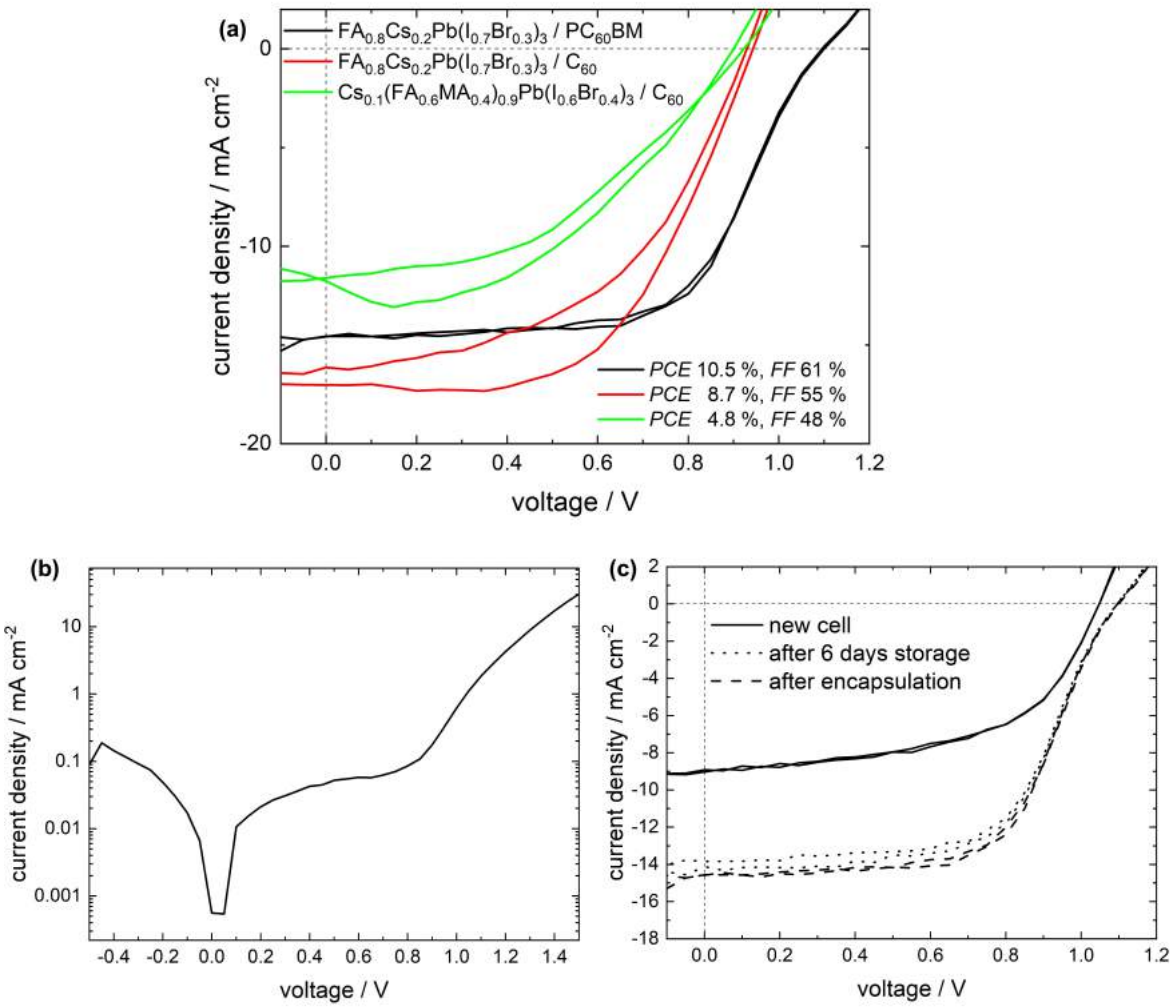

Figure 13: (a) *JV* curves of three perovskite/ETL combinations. (b) Dark *JV* curve of an ITO/PTAA/$FA_{0.8}Cs_{0.2}Pb(I_{0.7}Br_{0.3})_3$/$PC_{60}BM$/BCP/Ag solar cell. A leakage current of 0.02 mA cm^{-2} at 0.2 V is apparent. (c) *JV* curves of the directly prepared $FA_{0.8}Cs_{0.2}Pb(I_{0.7}Br_{0.3})_3$/$PC_{60}BM$ solar cell and after 6 days storage in a glove box and after encapsulation.

Table 6: V_{OC}, J_{SC}, *FF*, and *PCE* of the best best performing cell of different perovskite/ETL configurations in solar cells.

perovskite/ETL	scan	V_{OC} / V	J_{SC} / mA cm^{-2}	*FF* / %	*PCE* / %
$FA_{0.8}Cs_{0.2}Pb(I_{0.7}Br_{0.3})_3$/$PC_{60}BM$	forw.	1.10	14.6	58	10.0
	rev.	1.10	14.6	61	10.5
$FA_{0.8}Cs_{0.2}Pb(I_{0.7}Br_{0.3})_3$/$C_{60}$	forw.	0.93	16.1	49	7.3
	rev.	0.94	17.0	55	8.7
$Cs_{0.1}(FA_{0.6}MA_{0.4})_{0.9}Pb(I_{0.6}Br_{0.4})_3$/$C_{60}$	forw.	0.92	11.2	41	4.1
	rev.	0.90	11.4	48	4.8

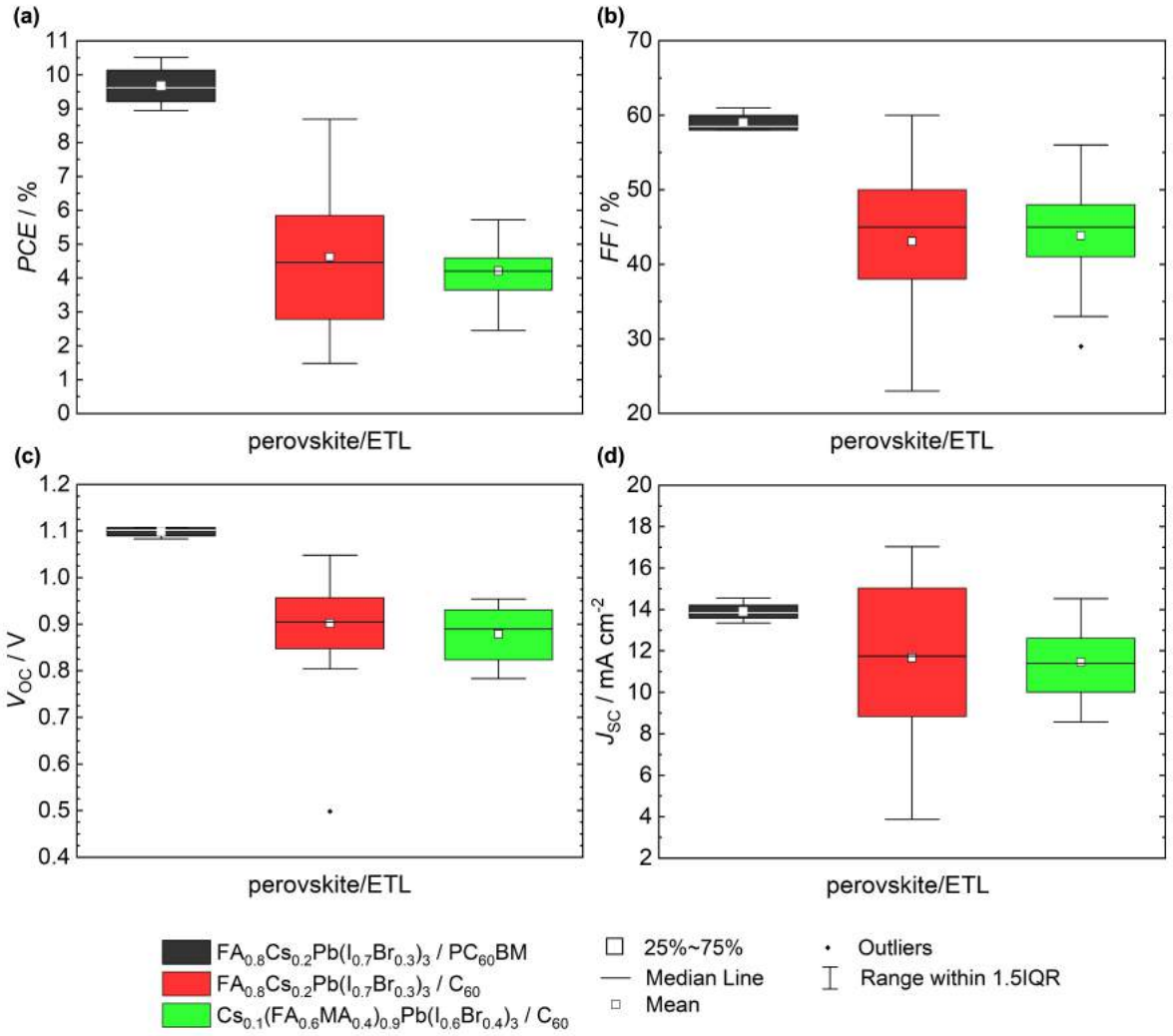

Figure 14: (a) *PCE*, (b) *FF*, (c) V_{OC} and (d) J_{SC} box plot of the three perovskite/ETL composites with the 1.5 fold Interquartile range, the upper and lower quartile, the median value, the mean value and outliers.

Figure 13 (b) shows the dark semi-log *JV*-plot of an encapsulated double-cation/ $PC_{60}BM$ solar cell for the determination of the leakage current. Leakage current, which is notable at low voltages, can be a consequence of undesired non radiative recombination effects, poor morphology of the perovskite and interfacial problems in thin film solar cells [24, 39, 107, 108]. In this thesis, for the optimized solar cell a value of 0.02 $mA\,cm^{-2}$ at 0.2 V was achieved, which is between the values of a MAPI solar cell (10.9 % *PCE*) of 0.45 $mA\,cm^{-2}$ at 0.2 V [24] and the value of a mixed-cation PSC (17.3 % *PCE*) of $2.7*10^{-6}$ $mA\,cm^{-2}$ at 0.2 V [31].

Figure 13 (c) shows the storage effect of 6 days in a glove box and the encapsulation effect onto the performance of an encapsulated $FA_{0.8}Cs_{0.2}Pb(I_{0.7}Br_{0.3})_3/PC_{60}BM$ device. During the 6 days storage, the oxygen concentration in the glove box increased from 5 ppm to over 200 ppm for 2 days for unknown reasons. A significant current

density increase from $\sim$9 mA cm^{-2} to $\sim$15 mA cm^{-2} was observed after 6 days storage of the original cell. Also the open-circuit voltage increased by approx. 0.05 V. The origin for this dramatic increase in performance is unknown. However, it was reported that storage under ambient conditions increased the V_{OC} of PSCs because of defect passivation at the perovskite/HTL interface and reduction of perovskite surface recombination [109, 110].

Figure 14 (a) - (d) summarizes the results of the produced solar cells in form of a box plot for *PCE*, *FF*, V_{OC} and J_{SC}. It has to be noted that only solar cells reaching at least 50 % of the *FF* of the best solar cell of a batch are defined as working and are displayed in figure 14 (a) - (d). The best solar cell is defined as the device with the highest *PCE* of a batch. The $FA_{0.8}Cs_{0.2}Pb(I_{0.7}Br_{0.3})_3$/$PC_{60}BM$ solar cells clearly outperformed the alternative with C_{60} and the triple-cation perovskite/C_{60} cells with a *PCE* mean value of 9.7 % vs. 4.7 % and 4.2 %, but also with a mean *FF* of 59 % vs. 43 % and 44 % and a mean V_{OC} of 1.10 V vs. 0.90 V and 0.88 V. It was noticed that in figure 14 (d) the $FA_{0.8}Cs_{0.2}Pb(I_{0.7}Br_{0.3})_3$/$C_{60}$ combination had the highest J_{SC} with 17.0 mA cm^{-2} and the widest 1.5 fold interquartile range (IQR) from 17.0 mA cm^{-2} to 3.9 mA cm^{-2}. This can be explained because of the high number of 240 produced solar cells with this recipe.

3.2.3 External quantum efficiency measurement and surface morphology

Figure 15 (a) shows the *EQE* plot and the integral of the current density calculated from *EQE* for an ITO/PTAA/$FA_{0.8}Cs_{0.2}Pb(I_{0.7}Br_{0.3})_3$/$PC_{60}BM$/BCP/Ag solar cell. Between 400 nm and 680 nm an external quantum efficiency between 71.6 % and 81.6 % was reached. Perovskite recipes with band gaps between 1.72 eV and 1.74 eV achieved in the same wavelength period *EQEs* from $\sim$ 75 % - 90 % [21], from $\sim$ 82 % - 94 % [111] and from $\sim$ 73 % - 85 % [34]. A descent of the *EQE* from 71.6 % at 680 nm to 5.8 % at 730 nm was observed. For the examined wavelength range from 350 nm to 800 nm, a current integral of 15.9 mA cm^{-2} was obtained. This was more than the short circuit current of the produced solar cell with 14.6 mA cm^{-2}. This deviation can be partly explained due to an error in measuring the area of the cell.

Figure 15 (b) shows a SEM image of a $FA_{0.8}Cs_{0.2}Pb(I_{0.7}Br_{0.3})_3$ perovskite film on PTAA/quartz glass. Perovskite grains with a large sized distribution with a maximum diameter size of $\sim$ 1.5 µm were apparent, whereas the smallest sizes were not determinable with 1000 fold magnitude. Small grain sizes in perovskite layers lead to a decreased PSC performance, a poor stability, more surface defects and to a rise in open-circuit voltage deficit [8, 48, 112]. Also, pinholes were observed that lead to direct contact between the ETL and the HTL and decrease the performance of

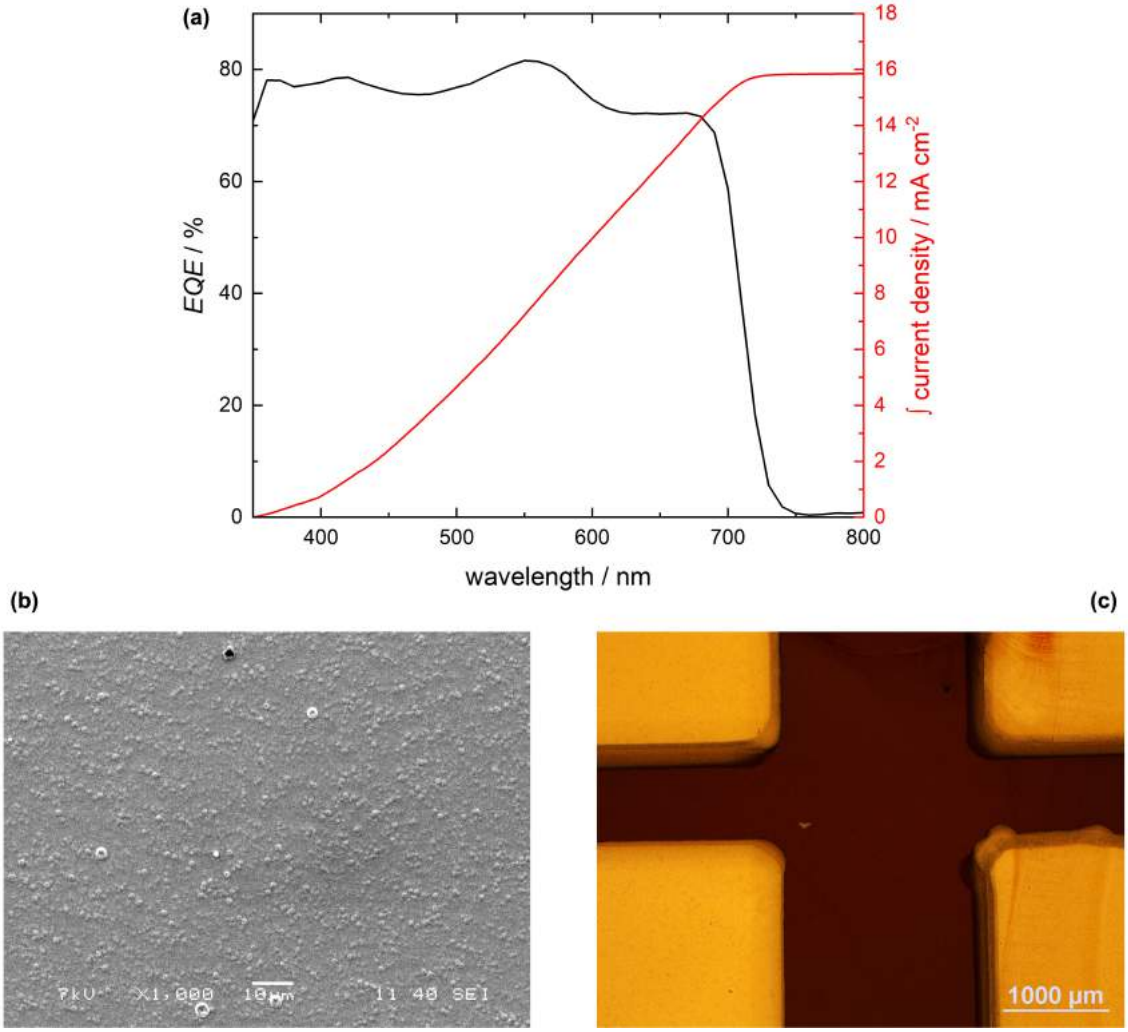

Figure 15: (a) The *EQE* and the integral of current density of a solar cell composition containing a $FA_{0.8}Cs_{0.2}Pb(I_{0.7}Br_{0.3})_3/PC_{60}BM$ combination. (b) A SEM image of a $PTAA/FA_{0.8}Cs_{0.2}Pb(I_{0.7}Br_{0.3})_3$ film with 1000 fold magnitude and 7 kV acceleration. (c) A light microscope image of a $FA_{0.8}Cs_{0.2}Pb(I_{0.7}Br_{0.3})_3/C_{60}$ solar cell composition of the bottom centre.

the PSC [113, 114]. Both phenomena suggest that the perovskite layer processing method needs to be further optimized. The thickness of the perovskite/PTAA film has been obtained with a profilometer and an average thickness of 345 nm $\pm$ 12 nm (95 % confidence interval, n = 3) was achieved, where the PTAA layer occupied a thickness of $\sim$10 nm. Additionally, the thickness and the surface roughness of a $PTAA/FA_{0.8}Cs_{0.2}Pb(I_{0.7}Br_{0.3})_3/C_{60}/BCP$ film was detected with 379 nm $\pm$ 13 nm (95 % confidence interval, n = 5) and 26 nm $\pm$ 13 nm (95 % confidence interval, n = 5), respectively. In figure 15 (c) an uniform coverage of the perovskite on the substrate was observed. The light microscope image showed that a deformation of the silver electrode contacts was apparent. This indicates that the fixation of the solar cells in

the shadow mask in the silver thermal evaporation process needs to be improved in order to improve performance and stability of the device.

3.2.4 Photoluminescence and electroluminescence measurement results

Time dependent photoluminescence spectra were recorded for an encapsulated ITO/PTAA/$FA_{0.8}Cs_{0.2}Pb(I_{0.7}Br_{0.3})_3$/$PC_{60}BM$/BCP/Ag solar cell. Figure 16 (a) demonstrates the time dependence of the *PL* spectrum under continuous irradiation with a 532 nm laser. At the start of illumination a clear signal at 719 nm was apparent, which was consistent with the determined band gap of 717 nm by PDS for this perovskite composition. Interestingly, a second peak appeared at 762 nm after 300 s illumination and shifted to 768 nm after 720 s illumination. According to the calculations in [52] and section 3.1.1, these wavelengths corresponded to a bromide content of 14 % to 10 %. The formation of new red-shifted peak indicated a photo induced phase segregation with a iodide-rich, narrow band gap sub phase. The peak formation and the *PL* red shift over time is reported for wide-band gap mixed halide perovskites near grain boundaries and interfaces after prolonged illumination [15, 49, 53, 55, 115]. The iodide-rich minority is assumed to act as recombination center trap for trap-mediated recombination [58, 70, 110].
Figure 16 (b) shows a *PL* curve of the PSC after 120 s illumination with a 532 nm laser, as in figure (a) an additional red-shifted peak at 756 nm occurs. To test the reversibility of this effect, the material was left 15 s at the dark and was subsequently illuminated and measured. A distinct increase of the original perovskite signal at 719 nm in relation to sub signal at 756 nm was apparent. This indicated reversible light-induced phase segregation of mixed halides, similar to the fully reversible phase segregation after leaving perovskite under the dark for a few minutes, which was reported in [56, 58, 117]. Figure 16 (c) shows the *EL* spectrum of the PSC, which exhibited a distinct signal at 716 nm. This was approximately the same wavelength of the photoluminescence peak, which proved that *EL* and *PL* shared the same origin, namely the recombination of free electron-hole pairs via the same recombination state.

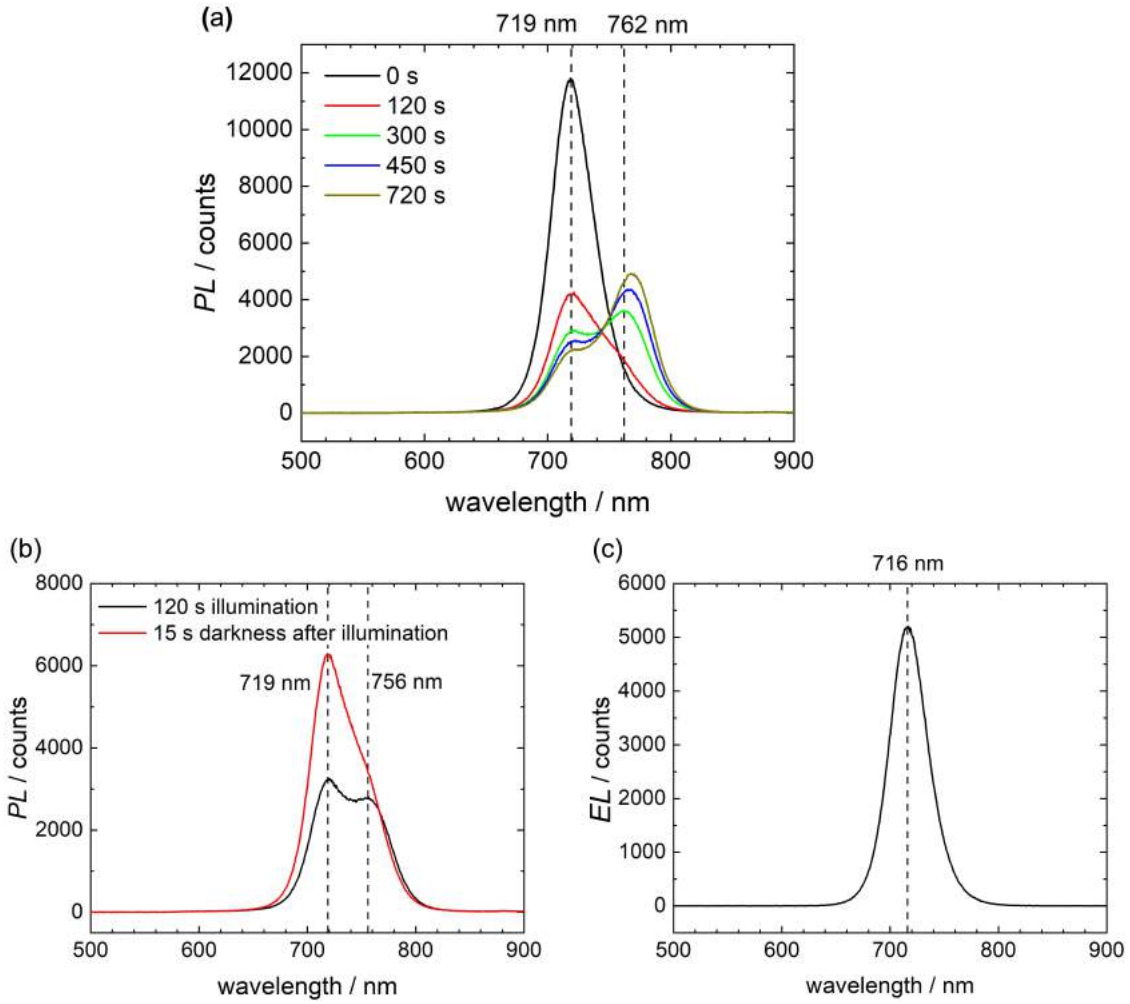

Figure 16: (a) ITO/PTAA/$FA_{0.8}Cs_{0.2}Pb(I_{0.7}Br_{0.3})_3$/$PC_{60}BM$/BCP/Ag photoluminescence time dependence under continuous irradiation with a 5 mW - 532 nm laser, a slit with of 100 µm and an exposure time of 1 s. (b) *PL* spectra of the PSC after 120 s irradiation with 5 mW and 532 nm (on a different spot) and after 15 s in the darkness and resumption of the illumination. (c) *EL* spectrum of the PSC recorded at a slit width of 1000 µm, an exposure time of 3 s and input of 0.75 mA at 1.4 V.

4 Conclusion and outlook

In this thesis, a recipe and manufacturing procedure for a processable and efficient perovskite solar cell with a large band gap was developed. The key points of the implementation of this aim were to provide a stable hole transport layer (PTAA) for the deposition of perovskite layers, experimenting with composition and solubility of the perovskite precursor, observing the influence of the type of antisolvent, comparing different types of electron transport layers and further optimizations. In PDS experminents the direct influence of the bromide fraction of a $FA_{0.8}Cs_{0.2}Pb(I_{1-x}Br_x)_3$ perovskite film onto the band gap was observed. By increasing the bromide content x from 0 to 0.5, the E_g increased from 1.57 eV to 1.84 eV, which shows the advantageous bandgap tunability of mixed-halide perovskites. In the PDS spectra an additional shoulder for the perovskite with 30% - 50% was detected. Similarly in the *PL* spectra for the same perovskites, an additional peak or peak broadening was observed. This indicates that for the perovskite with 30 % Br and an E_g of 1.73 eV a transition from photo-stability to photo-instability segregation occurs, which is in accordance to the literature. The photo-instability is caused by light-induced phase segregation. This led to the conclusion that with this recipe and this processing procedure the highest possible band gap for achieving a photostable PSC is $\sim$1.7 eV, without the usage of specific passivating or defect-reducing reagents.
The best PSC, with the configuration ITO/PTAA/$FA_{0.8}Cs_{0.2}Pb(I_{0.7}Br_{0.3})_3$/$PC_{60}$BM/BCP/-Ag (encapsulated), achieved a *PCE* of 10.5 %, a *FF* of 61 %, an J_{SC} of 14.6 mA cm^{-2} and a V_{OC} of 1.10 V. However, a decrease of *PCE* to 5.6 % was observed after 10 min illumination. The largest number of produced solar cells (240) consisted of a $FA_{0.8}Cs_{0.2}Pb(I_{0.7}Br_{0.3})_3/C_{60}$ configuration. C_{60} is beneficial for the use in TSCs, because it can be packed densely and is deposited by thermal evaporation. With this configuration an J_{SC} as high as 17.0 mA cm^{-2} was achieved, however high J_{SC} are undesired for WBG sub cell in tandem solar cells due to the current match requirement. An alternative triple-cation perovskite recipe based on a $Cs_{0.1}(FA_{0.6}MA_{0.4})_{0.9}Pb(I_{0.6}Br_{0.4})_3/C_{60}$ composition with a *FF* of 48 % and a *PCE* of 4.8 % was not able to compete with the top performance device. Further improvement of the processing procedure would be required.
The $FA_{0.8}Cs_{0.2}Pb(I_{0.7}Br_{0.3})_3$/$PC_{60}$BM PSC showed an *EQE* ranging from 71.6 % to 81.6 % between 400 nm and 680 nm. The perovskite layer exhibited a thickness of 335 nm and large distribution of grain sizes, where the largest diameter was $\sim$1.5 µm. For the PSC a distinctive *EL* signal at 716 nm was detected. After 120 s illumination 2 *PL* peaks were observed at 719 nm and 756 nm, where the latter signal was significantly reduced after leaving the sample 15 s in the darkness, which is an indication

for reversible photo-induced phase segregation.

In summary, processable and efficient perovskite solar cells with a large band gap were produced. Upon illumination, the Hoke effect, the photo induced phase segregation occurred for perovskites with high Br concentrations. In order to be insertable in a tandem solar cell, the implemented PSC recipe and manufacturing process needs to optimized towards a perovskite layer with increased grain size and a reduced defect- and trap-density by e.g. solvent engineering or by passivation with 2D layers or additives. It has been observed that absolute cleanliness and an environment free of solvents is of highest importance in the glovebox.

5 Appendix

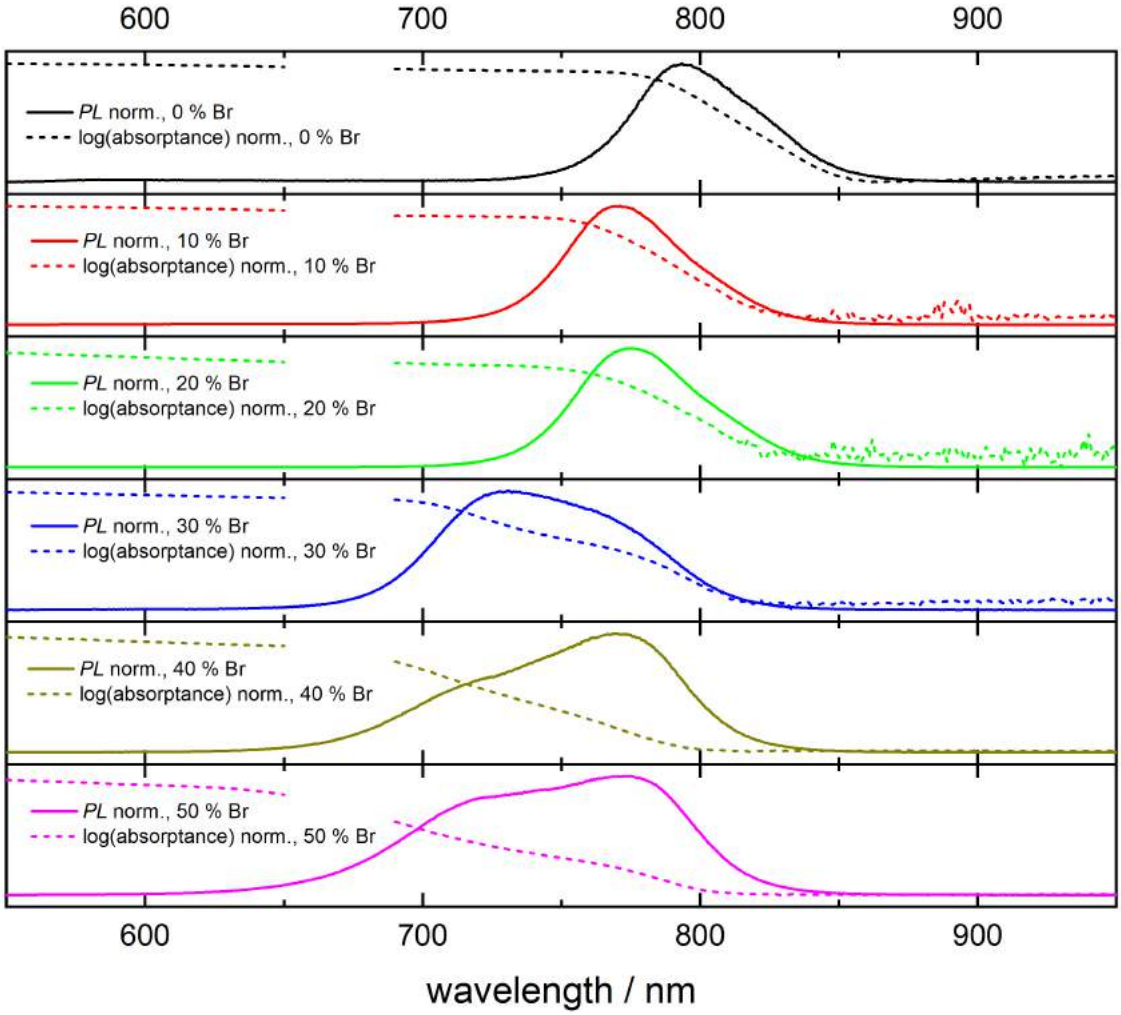

Figure 17: Comparison of normalised *PL* spectra and PDS absorptance spectra of $FA_{0.8}Cs_{0.2}Pb(I_{1-x}Br_x)_3$ thin films with varying bromide mole fraction x. The *PL* samples were measured under vacuum.

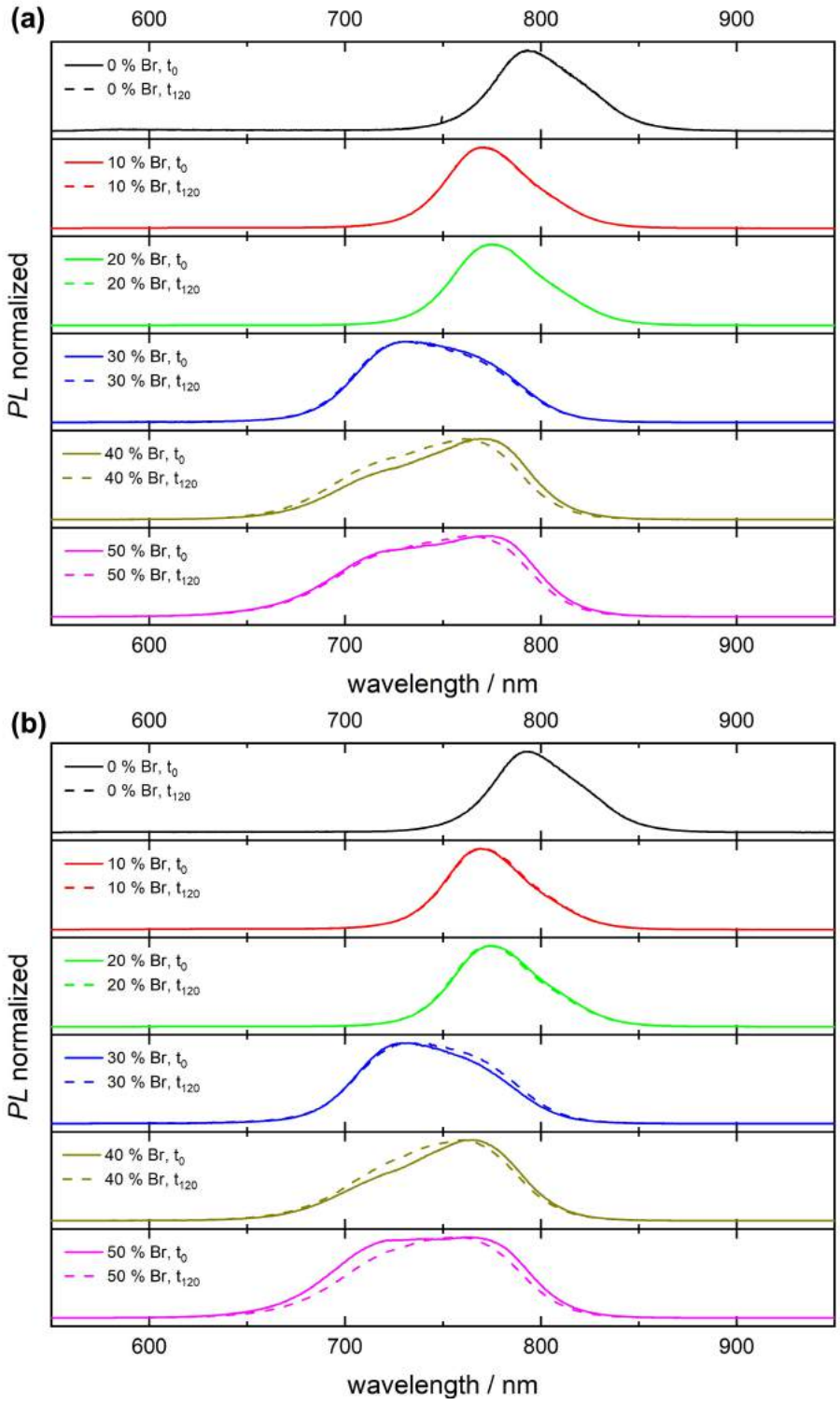

Figure 18: *PL* analysis of $FA_{0.8}Cs_{0.2}Pb(I_{1-x}Br_x)_3$ thin films with varying bromide mole fraction x. The spectra were measured under vacuum (a) and under atmospheric conditions (b) . The *PL* of the perovskites was determined directly after the start of illumination (t_0) and after 120 s (t_{120}). The signals were recorded with slit widths of 250 µm - 1000 µm and exposure times of 0.5 s - 1 s.

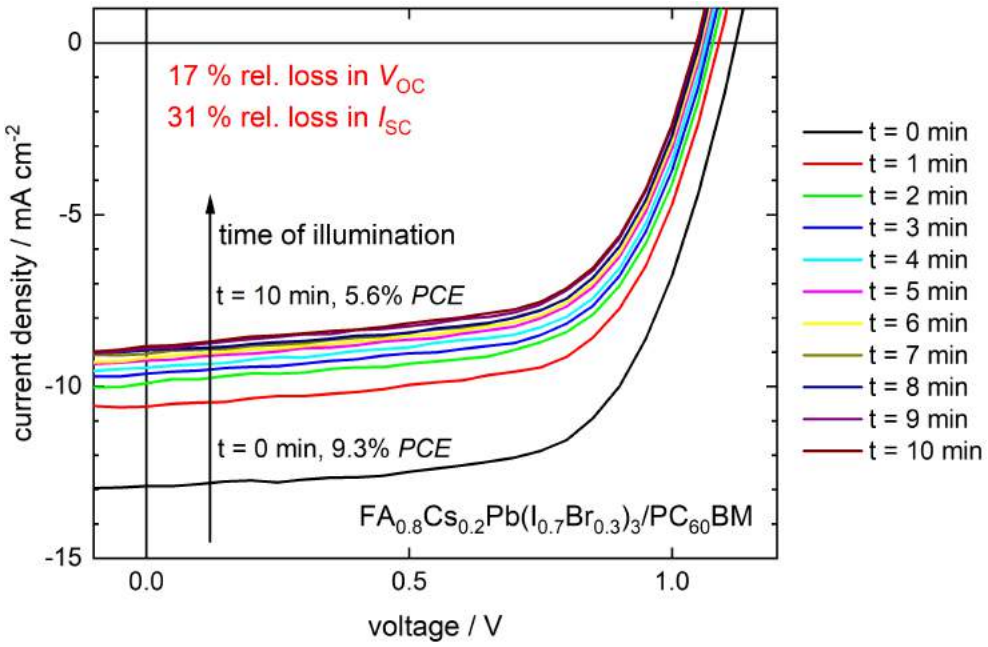

Figure 19: Decrease of the *PCE* from 9.3 % to 5.6 % for a $FA_{0.8}Cs_{0.2}Pb(I_{0.7}Br_{0.3})_3/PC_{60}BM$ PSC after 10 min continuos illumination with a xenon arc lamp. The PSC was stored 4 month in an inert atmosphere prior to the measurement.

List of abbreviations

BCP	Bathocuproine
C_{60}	Fullerene-C_{60}
CB	Conduction band
CCD	Charge-coupled device
CTL	Charge transport layer
DMF	Dimethylformamide
E_g	Bandgap
EL	Electroluminescence
EQE	External quantum efficiency
ETL	Electron transport layer
FF	Fill factor
HCl	Hydrochloric acid
HOMO	Highest occupied molecule orbital
HTL	Hole transport layer
LED	Light-emitting diode
LUMO	Lowest occupied molecule orbital
J_{SC}	Short-circuit current density
ITO	Indium tin oxide
JV	Current density-voltage
MA	Methylammonium
NIR	Near infrared
OIHP	Organic-inorganic halide perovskites
OSC	Organic solar cell
PCE	Power conversion efficiency
PDS	Photothermal deflection spectroscopy
PEDOT:PSS	Poly(3,4-ethylenedioxythiophene):poly-(styrenesulfonate)
PL	Photoluminescence
PMT	Photomultiplier tube
PSC	Perovskite solar cell
PTAA	Poly-bis(4-phenyl)(2,4,6-trimethylphenyl)amine
PV	Photovoltaic
SEM	Scanning electron microscopy
TSC	Tandem solar cell
VB	Valence band
V_{OC}	Open-circuit voltage
WBG	Wide-band gap
XRD	X-ray diffraction

List of figures

List of tables

References

[1] IEA, IEA statistics, `https://www.iea.org/` (visited on 12/12/2021).

[2] V. Quaschning, *Erneuerbare Energien und Klimaschutz*, 5th ed., Hanser, München, **2020**, pp. 1–167.

[3] K. Mertens, *Photovoltaik - Lehrbuch zu Grundlagen, Technologie und Praxis*, 5th ed., Hanser, München, **2020**, p. 162.

[4] L. Gao, I. Spanopoulos, W. Ke, S. Huang, I. Hadar, L. Chen, X. Li, G. Yang, M. G. Kanatzidis, *ACS Energy Lett.* **2019**, *4*, 1763–1769.

[5] B. Xu, Z. Zhu, J. Zhang, H. Liu, C. C. Chueh, X. Li, A. K. Jen, *Adv. Energy Mater.* **2017**, *7*, 1–10.

[6] D. P. McMeekin, G. Sadoughi, W. Rehman, G. E. Eperon, M. Saliba, M. T. Hörantner, A. Haghighirad, N. Sakai, L. Korte, B. Rech, M. B. Johnston, L. M. Herz, H. J. Snaith, *Science* **2016**, *351*, 151–155.

[7] H. Min, M. Kim, S. U. Lee, H. Kim, G. Kim, K. Choi, J. H. Lee, S. I. Seok, *Science* **2019**, *366*, 749–753.

[8] J. W. Lee, S. H. Bae, N. De Marco, Y. T. Hsieh, Z. Dai, Y. Yang, *Mater. Today Energy* **2018**, *7*, 149–160.

[9] A. Kojima, K. Teshima, Y. Shirai, T. Miyasaka, *J. Am. Chem. Soc.* **2009**, *131*, 6050–6051.

[10] J. Jeong, M. Kim, J. Seo, H. Lu, P. Ahlawat, A. Mishra, Y. Yang, M. A. Hope, F. T. Eickemeyer, M. Kim, Y. J. Yoon, I. W. Choi, B. P. Darwich, S. J. Choi, Y. Jo, J. H. Lee, B. Walker, S. M. Zakeeruddin, L. Emsley, U. Rothlisberger, A. Hagfeldt, D. S. Kim, M. Grätzel, J. Y. Kim, *Nature* **2021**, *592*, 381–385.

[11] M. Safdari, A. Hagfeldt in *Charact. Tech. Perovskite Sol. Cell Mater.* Elsevier, **2019**, pp. 237–254.

[12] W. Shockley, H. J. Queisser, *J. Appl. Phys.* **1961**, *32*, 510–519.

[13] M. Rai, L. H. Wong, L. Etgar, *J. Phys. Chem. Lett.* **2020**, *11*, 8189–8194.

[14] J. Chen, L. Zuo, Y. Zhang, X. Lian, W. Fu, J. Yan, J. Li, G. Wu, C. Z. Li, H. Chen, *Adv. Energy Mater.* **2018**, *8*, 1–10.

[15] Z. Li, T. H. Kim, S. Y. Han, Y. J. Yun, S. Jeong, B. Jo, S. A. Ok, W. Yim, S. H. Lee, K. Kim, S. Moon, J. Y. Park, T. K. Ahn, H. Shin, J. Lee, H. J. Park, *Adv. Energy Mater.* **2020**, *10*, 1–16.

[16] P. Li, X. Liu, Y. Zhang, C. Liang, G. Chen, F. Li, M. Su, G. Xing, X. Tao, Y. Song, *Angew. Chemie - Int. Ed.* **2020**, *59*, 6909–6914.

[17] C. D. Bailie, M. D. McGehee, *MRS Bull.* **2015**, *40*, 681–685.

[18] S. G. Prolongo, A. D. Printz, N. Rolston, B. L. Watson, R. H. Dauskardt, *Thin Solid Films* **2018**, *646*, 61–66.

[19] D. B. Khadka, Y. Shirai, M. Yanagida, T. Noda, K. Miyano, *ACS Appl. Mater. Interfaces* **2018**, *10*, 22074–22082.

[20] M. Stolterfoht, C. M. Wolff, Y. Amir, A. Paulke, L. Perdigón-Toro, P. Caprioglio, D. Neher, *Energy Environ. Sci.* **2017**, *10*, 1530–1539.

[21] C. Chen, Z. Song, C. Xiao, R. A. Awni, C. Yao, N. Shrestha, C. Li, S. S. Bista, Y. Zhang, L. Chen, R. J. Ellingson, C. S. Jiang, M. Al-Jassim, G. Fang, Y. Yan, *ACS Energy Lett.* **2020**, *5*, 2560–2568.

[22] D. Kim, H. J. Jung, I. J. Park, B. W. Larson, S. P. Dunfield, C. Xiao, J. Kim, J. Tong, P. Boonmongkolras, S. G. Ji, F. Zhang, S. R. Pae, M. Kim, S. B. Kang, V. Dravid, J. J. Berry, J. Y. Kim, K. Zhu, D. H. Kim, B. Shin, *Science* **2020**, *368*, 155–160.

[23] J. Y. Ye, J. Tong, J. Hu, C. Xiao, H. Lu, S. P. Dunfield, D. H. Kim, X. Chen, B. W. Larson, J. Hao, K. Wang, Q. Zhao, Z. Chen, H. Hu, W. You, J. J. Berry, F. Zhang, K. Zhu, *Sol. RRL* **2020**, *4*, 1–8.

[24] K. Tvingstedt, L. Gil-Escrig, C. Momblona, P. Rieder, D. Kiermasch, M. Sessolo, A. Baumann, H. J. Bolink, V. Dyakonov, *ACS Energy Lett.* **2017**, *2*, 424–430.

[25] T. Todorov, T. Gershon, O. Gunawan, Y. S. Lee, C. Sturdevant, L. Y. Chang, S. Guha, *Adv. Energy Mater.* **2015**, *5*, 1–6.

[26] X. Chen, Z. Jia, Z. Chen, T. Jiang, L. Bai, F. Tao, J. Chen, X. Chen, T. Liu, X. Xu, C. Yang, W. Shen, W. E. Sha, H. Zhu, Y. Yang, *Joule* **2020**, *4*, 1594–1606.

[27] A. Rajagopal, Z. Yang, S. B. Jo, I. L. Braly, P. W. Liang, H. W. Hillhouse, A. K. Jen, *Adv. Mater.* **2017**, *29*, 1–10.

[28] C. Chen, F. Li, L. Zhu, Z. Shen, Y. Weng, Q. Lou, F. Tan, G. Yue, Q. Huang, M. Wang, *Nano Energy* **2020**, *68*, 1–11.

[29] S. Song, G. Kang, L. Pyeon, C. Lim, G. Y. Lee, T. Park, J. Choi, *ACS Energy Lett.* **2017**, *2*, 2667–2673.

[30] S. S. Mali, C. K. Hong, *Nanoscale* **2016**, *8*, 10528–10540.

[31] B. Hailegnaw, V. Poscher, C. Ulbricht, H. Seelajaroen, I. Teasdale, Y. Salinas, N. S. Sariciftci, M. C. Scharber, *Phys. Status Solidi Appl. Mater. Sci.* **2019**, *216*, 1–10.

[32] V. M. Caselli, Z. Wei, M. M. Ackermans, E. M. Hutter, B. Ehrler, T. J. Savenije, *ACS Energy Lett.* **2020**, *5*, 3821–3827.

[33] K. O. Brinkmann, T. Becker, F. Zimmermann, T. Gahlmann, C. Koch, D. Hertel, H.-z. Berlin, L. Merten, F. Schreiber, **2020**, *5*, 1–16.

[34] Z. Li, S. Wu, J. Zhang, K. C. Lee, H. Lei, F. Lin, Z. Wang, Z. Zhu, A. K. Jen, *Adv. Energy Mater.* **2020**, *10*, 1–9.

[35] D. P. McMeekin, S. Mahesh, N. K. Noel, M. T. Klug, J. C. Lim, J. H. Warby, J. M. Ball, L. M. Herz, M. B. Johnston, H. J. Snaith, *Joule* **2019**, *3*, 387–401.

[36] L. Liu, Z. Xiao, C. Zuo, L. Ding, *J. Semicond.* **2021**, *42*, 1–4.

[37] Q. Zeng, L. Liu, Z. Xiao, F. Liu, Y. Hua, Y. Yuan, L. Ding, *Sci. Bull.* **2019**, *64*, 885–887.

[38] K. Lang, Q. Guo, Z. He, Y. Bai, J. Yao, M. Wakeel, M. S. Alhodaly, T. Hayat, Z. Tan, *J. Phys. Chem. Lett.* **2020**, *11*, 9596–9604.

[39] M. Ye, C. He, J. Iocozzia, X. Liu, X. Cui, X. Meng, M. Rager, X. Hong, X. Liu, Z. Lin, *J. Phys. D. Appl. Phys.* **2017**, *50*, 1–16.

[40] C. Chen, S. Zhang, S. Wu, W. Zhang, H. Zhu, Z. Xiong, Y. Zhang, W. Chen, *RSC Adv.* **2017**, *7*, 35819–35826.

[41] D. Luo, R. Su, W. Zhang, Q. Gong, R. Zhu, *Nat. Rev. Mater.* **2020**, *5*, 44–60.

[42] M. Cheng, C. Zuo, Y. Wu, Z. Li, B. Xu, Y. Hua, L. Ding, *Sci. Bull.* **2020**, *65*, 1237–1241.

[43] D. Ritter, K. Weiser, *Opt. Commun.* **1986**, *57*, 336–338.

[44] M. I. Pech-Canul, N. M. Ravindra in *Semicond. Synth. Prop. Appl.* Springer-Verlag, **2019**, pp. 102–104.

[45] F. Mayr, MSc Thesis, Johannes Kepler Universität Linz, **2020**.

[46] W. Li, K. Zhao, H. Zhou, W. Yu, J. Zhu, Z. Hu, J. Chu, *J. Phys. D. Appl. Phys.* **2019**, *52*, 1–6.

[47] J. Jimenez, J. Tomm, *Spectroscopic Analysis of Optoelectronic Semiconductors*, *Vol. 202*, **2016**, pp. 1–48.

[48] C. Chen, Z. Song, C. Xiao, D. Zhao, N. Shrestha, C. Li, G. Yang, F. Yao, X. Zheng, R. J. Ellingson, C. S. Jiang, M. Al-Jassim, K. Zhu, G. Fang, Y. Yan, *Nano Energy* **2019**, *61*, 141–147.

[49] C. Tao, G. Fang, J. Liang, C. Chen, X. Hu, Z. Chen, X. Zheng, J. Li, H. Wang, F. Ye, M. Xiao, Z. Lu, Y. Xu, S. Zhang, R. Yu, *ACS Appl. Mater. Interfaces* **2020**, *12*, 48458–48466.

[50] F. Penã-Camargo, P. Caprioglio, F. Zu, E. Gutierrez-Partida, C. M. Wolff, K. Brinkmann, S. Albrecht, T. Riedl, N. Koch, D. Neher, M. Stolterfoht, *ACS Energy Lett.* **2020**, *5*, 2728–2736.

[51] J. Xu, C. C. Boyd, Z. J. Yu, A. F. Palmstrom, D. J. Witter, B. W. Larson, R. M. France, J. Werner, S. P. Harvey, E. J. Wolf, W. Weigand, S. Manzoor, M. F. Van Hest, J. J. Berry, J. M. Luther, Z. C. Holman, M. D. McGehee, *Science* **2020**, *367*, 1097–1104.

[52] J. H. Noh, S. H. Im, J. H. Heo, T. N. Mandal, S. I. Seok, *Nano Lett.* **2013**, *13*, 1764–1769.

[53] K. A. Bush, K. Frohna, R. Prasanna, R. E. Beal, T. Leijtens, S. A. Swifter, M. D. McGehee, *ACS Energy Lett.* **2018**, *3*, 428–435.

[54] W. Mao, C. R. Hall, S. Bernardi, Y. B. Cheng, A. Widmer-Cooper, T. A. Smith, U. Bach, *Nat. Mater.* **2021**, *20*, 55–61.

[55] W. Li, M. U. Rothmann, A. Liu, Z. Wang, Y. Zhang, A. R. Pascoe, J. Lu, L. Jiang, Y. Chen, F. Huang, Y. Peng, Q. Bao, J. Etheridge, U. Bach, Y. B. Cheng, *Adv. Energy Mater.* **2017**, *7*, 1–8.

[56] J. Wei, Q. Wang, J. Huo, F. Gao, Z. Gan, Q. Zhao, H. Li, *Adv. Energy Mater.* **2021**, *11*, 35–37.

[57] P. V. Kamat, M. Kuno, *Acc. Chem. Res.* **2021**, *54*, 520–531.

[58] E. T. Hoke, D. J. Slotcavage, E. R. Dohner, A. R. Bowring, H. I. Karunadasa, M. D. McGehee, *Chem. Sci.* **2015**, *6*, 613–617.

[59] H. Zhang, X. Fu, Y. Tang, H. Wang, C. Zhang, W. W. Yu, X. Wang, Y. Zhang, M. Xiao, *Nat. Commun.* **2019**, *10*, 1–8.

[60] X. Tang, M. Van Den Berg, E. Gu, A. Horneber, G. J. Matt, A. Osvet, A. J. Meixner, D. Zhang, C. J. Brabec, *Nano Lett.* **2018**, *18*, 2172–2178.

[61] M. C. Brennan, S. Draguta, P. V. Kamat, M. Kuno, *ACS Energy Lett.* **2018**, *3*, 204–213.

[62] G. F. Samu, C. Janaky, P. V. Kamat, *ACS Energy Lett.* **2017**, *2*, 1860–1861.

[63] D. J. Slotcavage, H. I. Karunadasa, M. D. McGehee, *ACS Energy Lett.* **2016**, *1*, 1199–1205.

[64] A. J. Knight, J. B. Patel, H. J. Snaith, M. B. Johnston, L. M. Herz, *Adv. Energy Mater.* **2020**, *10*, 1–11.

[65] J. B. Hoffman, A. L. Schleper, P. V. Kamat, *J. Am. Chem. Soc.* **2016**, *138*, 8603–8611.

[66] W. Rehman, D. P. McMeekin, J. B. Patel, R. L. Milot, M. B. Johnston, H. J. Snaith, L. M. Herz, *Energy Environ. Sci.* **2017**, *10*, 361–369.

[67] Z. Hu, Q. An, H. Xiang, L. Aigouy, B. Sun, Y. Vaynzof, Z. Chen, *ACS Appl. Mater. Interfaces* **2020**, *12*, 54824–54832.

[68] X. Wu, Y. Jiang, C. Chen, J. Guo, X. Kong, Y. Feng, S. Wu, X. Gao, X. Lu, Q. Wang, G. Zhou, Y. Chen, J. M. Liu, K. Kempa, J. Gao, *Adv. Funct. Mater.* **2020**, *30*.

[69] M. Hu, C. Bi, Y. Yuan, Y. Bai, J. Huang, *Adv. Sci.* **2015**, *3*, 6–11.

[70] A. J. Knight, L. M. Herz, *Energy Environ. Sci.* **2020**, *13*, 2024–2046.

[71] M. I. El-Henawey, I. M. Hossain, L. Zhang, B. Bagheri, R. Kottokkaran, V. L. Dalal, *J. Mater. Sci. Mater. Electron.* **2021**, *32*, 4067–4075.

[72] I. L. Braly, R. J. Stoddard, A. Rajagopal, A. R. Uhl, J. K. Katahara, A. K. Jen, H. W. Hillhouse, *ACS Energy Lett.* **2017**, *2*, 1841–1847.

[73] G. E. Eperon, M. T. Hörantner, H. J. Snaith, *Nat. Rev. Chem.* **2017**, *1*, 1–18.

[74] J. F. Geisz, R. M. France, K. L. Schulte, M. A. Steiner, A. G. Norman, H. L. Guthrey, M. R. Young, T. Song, T. Moriarty, *Nat. Energy* **2020**, *5*, 326–335.

[75] M. A. Steiner, R. M. France, J. Buencuerpo, J. F. Geisz, M. P. Nielsen, A. Pusch, W. J. Olavarria, M. Young, N. J. Ekins-Daukes, *Adv. Energy Mater.* **2021**, *11*, 1–8.

[76] T. Leijtens, K. A. Bush, R. Prasanna, M. D. McGehee, *Nat. Energy* **2018**, *3*, 828–838.

[77] H. Li, W. Zhang, *Chem. Rev.* **2020**, *120*, 9835–9950.

[78] L. Liu, Z. Xiao, C. Zuo, L. Ding, *J. Semicond.* **2021**, *42*, 1–4.

[79] H. Aqoma, I. F. Imran, F. T. A. Wibowo, N. V. Krishna, W. Lee, A. K. Sarker, D. Y. Ryu, S. Y. Jang, *Adv. Energy Mater.* **2020**, *10*, 1–10.

[80] Q. Ou, X. Bao, Y. Zhang, H. Shao, G. Xing, X. Li, L. Shao, Q. Bao, *Nano Mater. Sci.* **2019**, *1*, 268–287.

[81] K. Lin, J. Xing, L. N. Quan, F. P. G. de Arquer, X. Gong, J. Lu, L. Xie, W. Zhao, D. Zhang, C. Yan, W. Li, X. Liu, Y. Lu, J. Kirman, E. H. Sargent, Q. Xiong, Z. Wei, *Nature* **2018**, *562*, 245–248.

[82] Y. Liu, J. Cui, K. Du, H. Tian, Z. He, Q. Zhou, Z. Yang, Y. Deng, D. Chen, X. Zuo, Y. Ren, L. Wang, H. Zhu, B. Zhao, D. Di, J. Wang, R. H. Friend, Y. Jin, *Nat. Photonics* **2019**, *13*, 760–764.

[83] Y. Li, Z. Chen, D. Liang, J. Zang, Z. Song, L. Cai, Y. Zou, X. Wang, Y. Wang, P. Li, X. Gao, Z. Ma, X. Mu, A. El-Shaer, L. Xie, W. Su, T. Song, B. Sun, *Adv. Opt. Mater.* **2021**, *9*, 1–9.

[84] A. R. Bowman, F. Lang, Y. H. Chiang, A. Jiménez-Solano, K. Frohna, G. E. Eperon, E. Ruggeri, M. Abdi-Jalebi, M. Anaya, B. V. Lotsch, S. D. Stranks, *ACS Energy Lett.* **2021**, *6*, 612–620.

[85] S. Manzoor, J. Haeusele, K. A. Bush, Z. J. Yu, M. D. McGehee, Z. C. Holman, *IEEE 7th World Conf. Photovolt. Energy Convers.* **2018**, 220–223.

[86] S. Wu, Y. Ye, M. Luo, L. Chen, *J. Opt. Soc. Am. B* **2018**, *35*, 1825.

[87] P. Wuerfel, U. Wuerfel, *Physics of Solar Cells*, 3rd ed., Wiley-VCH, Weinheim, **2016**, p. 173.

[88] M. R. Khan, M. A. Alam, *Appl. Phys. Lett.* **2015**, *107*, 1–5.

[89] J. Lee, S. J. Ko, M. Seifrid, H. Lee, B. R. Luginbuhl, A. Karki, M. Ford, K. Rosenthal, K. Cho, T. Q. Nguyen, G. C. Bazan, *Adv. Energy Mater.* **2018**, *8*, 1–6.

[90] G. E. Eperon, G. E. Eperon, T. Leijtens, K. A. Bush, R. Prasanna, T. Green, J. T.-w. Wang, D. P. Mcmeekin, G. Volonakis, R. L. Milot, R. May, A. Palmstrom, J. Daniel, R. A. Belisle, J. B. Patel, E. S. Parrott, R. J. Sutton, W. Ma, B. Conings, A. Babayigit, H.-g. Boyen, S. Bent, F. Giustino, M. Herz, M. B. Johnston, M. D. Mcgehee, H. J. Snaith, *Science* **2016**, *9717*, 1–10.

[91] J. Chen, Y. Xiong, Y. Rong, A. Mei, Y. Sheng, P. Jiang, Y. Hu, X. Li, H. Han, *Nano Energy* **2016**, *27*, 130–137.

[92] Y. H. Seo, E. C. Kim, S. P. Cho, S. S. Kim, S. I. Na, *Appl. Mater. Today* **2017**, *9*, 598–604.

[93] T. Sakurai, S. Toyoshima, H. Kitazume, S. Masuda, H. Kato, K. Akimoto, *J. Appl. Phys.* **2010**, *107*, 1–6.

[94] Hamamatsu Photonics, Si Photodiodes, `https://www.hamamatsu.com/resources/pdf/ssd/si_pd_kspd0001e.pdf` (visited on 12/06/2021).

[95] A. S. Pratiyush, S. Krishnamoorthy, R. Muralidharan, S. Rajan, D. N. Nath in *Gall. Oxide*, Elsevier Inc., Amsterdam, **2018**, Chapter 16, pp. 369–399.

[96] A. H. M. Smets, K. Jäger, O. Isabella, R. van Swaaij, M. Zeman, *Solar Energy: The Physics and Engineering of Photovoltaic Conversion, Technologies and Systems*, 1st ed., UIT Cambridge, Cambridge, **2016**, Chapter 9, pp. 117–119.

[97] S. De Wolf, J. Holovsky, S. J. Moon, P. Löper, B. Niesen, M. Ledinsky, F. J. Haug, J. H. Yum, C. Ballif, *J. Phys. Chem. Lett.* **2014**, *5*, 1035–1039.

[98] X. X. Bi, P. C. Eklund, J. G. Zhang, T. A. Perry, C. P. Beetz, *J. Mater. Res.* **1990**, *5*, 811–817.

[99] S. Tang, X. Xiao, J. Hu, B. Gao, H. Chen, Z. Peng, J. Wen, M. Era, D. Zou, *Chempluschem* **2020**, *85*, 240–246.

[100] N. Li, Z. Zhu, J. Li, A. K. Jen, L. Wang, *Adv. Energy Mater.* **2018**, *8*, 1–8.

[101] J. Y. Kim, J. W. Lee, H. S. Jung, H. Shin, N. G. Park, *Chem. Rev.* **2020**, *120*, 7867–7918.

[102] C. M. Sutter-Fella, Y. Li, M. Amani, J. W. Ager, F. M. Toma, E. Yablonovitch, I. D. Sharp, A. Javey, *Nano Lett.* **2016**, *16*, 800–806.

[103] M. J. Trimpl, A. D. Wright, K. Schutt, L. R. Buizza, Z. Wang, M. B. Johnston, H. J. Snaith, P. Müller-Buschbaum, L. M. Herz, *Adv. Funct. Mater.* **2020**, *30*, 1–12.

[104] G. J. A. Wetzelaer, M. Scheepers, A. M. Sempere, C. Momblona, J. Ávila, H. J. Bolink, *Adv. Mater.* **2015**, *27*, 1837–1841.

[105] K. Gugujonovic, MSc Thesis, Johannes Kepler Universität Linz, **2020**.

[106] A. D. Taylor, Q. Sun, K. P. Goetz, Q. An, T. Schramm, Y. Hofstetter, M. Litterst, F. Paulus, Y. Vaynzof, *Nat. Commun.* **2021**, *12*, 1–11.

[107] L. Zhang, X. Yang, Q. Jiang, P. Wang, Z. Yin, X. Zhang, H. Tan, Y. M. Yang, M. Wei, B. R. Sutherland, E. H. Sargent, J. You, *Nat. Commun.* **2017**, *8*, 1–8.

[108] R. Das, R. N. Choudhary, *Appl. Phys. A Mater. Sci. Process.* **2019**, *125*, 1–13.

[109] Z. Guo, A. K. Jena, I. Takei, M. Ikegami, A. Ishii, Y. Numata, N. Shibayama, T. Miyasaka, *Adv. Funct. Mater.* **2021**, *31*, 1–9.

[110] Y. Cho, H. D. Kim, J. Zheng, J. Bing, Y. Li, M. Zhang, M. A. Green, A. Wakamiya, S. Huang, H. Ohkita, A. W. Ho-Baillie, *ACS Energy Lett.* **2021**, *6*, 925–933.

[111] S. Gharibzadeh, B. Abdollahi Nejand, M. Jakoby, T. Abzieher, D. Hauschild, S. Moghadamzadeh, J. A. Schwenzer, P. Brenner, R. Schmager, A. A. Haghighirad, L. Weinhardt, U. Lemmer, B. S. Richards, I. A. Howard, U. W. Paetzold, *Adv. Energy Mater.* **2019**, *9*, 1–10.

[112] J. Zhang, Y. Fang, W. Zhao, R. Han, J. Wen, S. Liu, *Adv. Mater.* **2021**, *33*, 1–8.

[113] Y. Rong, Y. Hu, A. Mei, H. Tan, M. I. Saidaminov, S. I. Seok, M. D. McGehee, E. H. Sargent, H. Han, *Science* **2018**, *361*, 1–7.

[114] P. Kaienburg, P. Hartnagel, B. E. Pieters, J. Yu, D. Grabowski, Z. Liu, J. Haddad, U. Rau, T. Kirchartz, *J. Phys. Chem. C* **2018**, *122*, 27263–27272.

[115] J. Xu, C. C. Boyd, Z. J. Yu, A. F. Palmstrom, D. J. Witter, B. W. Larson, R. M. France, J. Werner, S. P. Harvey, E. J. Wolf, W. Weigand, S. Manzoor, M. F. Van Hest, J. J. Berry, J. M. Luther, Z. C. Holman, M. D. McGehee, *Science* **2020**, *367*, 1097–1104.

[116] S. Gharibzadeh, B. Abdollahi Nejand, M. Jakoby, T. Abzieher, D. Hauschild, S. Moghadamzadeh, J. A. Schwenzer, P. Brenner, R. Schmager, A. A. Haghighirad, L. Weinhardt, U. Lemmer, B. S. Richards, I. A. Howard, U. W. Paetzold, *Adv. Energy Mater.* **2019**, *9*, 1–10.

[117] U. B. Cappel, S. Svanström, V. Lanzilotto, F. O. Johansson, K. Aitola, B. Philippe, E. Giangrisostomi, R. Ovsyannikov, T. Leitner, A. Föhlisch, S. Svensson, N. Mårtensson, G. Boschloo, A. Lindblad, H. Rensmo, *ACS Appl. Mater. Interfaces* **2017**, *9*, 34970–34978.